Science
AAAS

Supplementary Materials for

Total organic carbon measurements reveal major gaps in petrochemical emissions reporting

Megan He *et al*.

Corresponding authors: John Liggio, john.liggio@ec.gc.ca; Drew R. Gentner, drew.gentner@yale.edu

Science **383**, 426 (2024)
DOI: 10.1126/science.adj6233

The PDF file includes:

Materials and Methods

Aircraft Campaign

As part of the Environment and Climate Change Canada Air Pollution program, the National Research Council (NRC) of Canada's Convair-580 research aircraft was used to make measurements above the Athabasca Oil Sands (OS) region in Alberta, Canada in April, June, and July 2018. The campaign consisted of a total of 30 flights around 17 different OS facilities. The aircraft flew in box patterns (henceforth called "box flights") at multiple altitudes around various surface and in-situ mining operations to derive overall facility organic emissions in a manner described previously (*10*, *15*, *16*, *20*). In addition to box flights, the aircraft also flew along straight-line paths at multiple altitudes to study the transformation of organic compounds at different distances downwind (up to ~120 km) in the OS-emitted plume (henceforth called "transformation flights"). The aircraft utilized real-time wind direction and speed data in order to intercept air parcels perpendicular to the plume axis, and flew back and forth to create "screens" capturing different altitudes at each prescribed downwind distance. The transformation flights were designed such that changes in composition between these screens can be attributed to changes in plume dilution and chemistry that occurred within a single air parcel, with the exceptions of note here being the last screen of Flights 25-26 and 29, which had surface mining and in-situ extraction sites, respectively, located upwind of the last screen. As such they are used to examine changes across the final two screens in Figure 3.

Real-time measurements were taken via online instrumentation to characterize gas- and/or particle-phase composition and characteristics, while discrete gas-phase hydrocarbon samples were concurrently collected for analysis with offline mass spectrometry. Sampling methods relevant to this work are described in the SI below in brief, with further details in previous literature (*18*).

Gas-Phase Measurements and Sample Collection

Total gas-phase organic carbon (TC) concentrations (ppmC) were obtained via measurements of CO_2, CO, and CH_4 made by a pair of onboard Cavity Ring Down (CRD) absorption instruments (Picarro G2401-m). Total gaseous organic carbon concentrations were determined by subtracting CO_2, CO, and CH_4 contributions measured by the analyzer without a platinum catalyst. Specifically, the sampled air passed through two channels, with one channel containing a platinum catalyst (heated to 650°C) which converted all species to CO_2 before the air entered a Picarro instrument. The second channel had no catalyst and sampled air directly into another Picarro instrument. Each Picarro instrument measured CO_2, CO, and CH_4, such that the total carbon in channel (1) containing the catalyst is expressed as:

$$TC(1) = CO_2(1) + CH_4(1) + CO(1)$$

Similarly, the total carbon in the ambient channel (i.e., no catalyst) is expressed as:

$$TC(2) = CO_2(2) + CH_4(2) + CO(2)$$

The final measure of total carbon (TC_{Final}) which excludes CH_4 and CO, and is used in the subsequent analysis, is given as:

$$TC_{Final} = TC(1) - TC(2)$$

The approach was adapted from that of Stockwell et al. (2018) and Veres et al. (2010) which converted all carbon species to CO_2 at 100% efficiency for laboratory experiments (*46–48*). The catalyst was enclosed in a resistively heated ½" O.D. x 12" long stainless steel tube mounted on the exterior of the aircraft. The reverse-facing orientation of the inlet and the lack of an unheated portion ensured that particle entrainment was minimal and that TC gaseous losses were negligible. Calibrations were conducted in flight using mixtures of CO, CO_2 and CH_4, traceable to NOAA Global Monitoring Laboratory standards, resulting in an uncertainty of approximately ±60 ppbv C for each channel and ±85 ppb C at the 3σ level for the TC difference determination. Standards were sampled 1-2 times per flight (at the beginning and end of each flight). Additional details on the TC methodology are provided elsewhere (see Hayden et al. 2022 for details) (*18*).

NO, NO_2 and NO_y were measured using commercial chemiluminescence instruments (Thermo Scientific). NO_y measurements (the sum of reactive nitrogen oxides) further utilized an external molybdenum converter (Thermo Scientific), which was heated to 325 °C and placed immediately next to the sampling point, in conjunction with a 42i-TL Analyzer. Details of the Thermo Scientific instruments which were modified to measure NO, NO_2 and NO_y separately and at high time resolution (1 sec) are described in detail elsewhere (*18*). NO_y is used to examine the TC/NO_y emission ratios across transformation and regional flights (e.g., Figure 4C) in order to be inclusive of any NO_x (i.e., $NO+NO_2$) emissions that may have reacted downwind to form other NO_y compounds. In this study, NO_y is quantified as NO_2 for consistency, and the use of NO_y in the ratios (particularly for downwind transformation flights) avoided potentially overestimating the ratios downwind if a portion of NO_x had been lost to chemical reactions (possibly up to 40% far downwind based on NO_x/NO_y ratios). However, this approach could have also biased the ratios low if some of the oxygen in NO_y was not from NO or NO_2. Emissions and emission ratios from box flights are calculated using NO_x (as the sum of NO and NO_2 measured separately) given the proximity to sources, although in this case, NO_x accounted for >90% of total NO_y.

A subset of VOCs (including OVOCs) was measured via a Proton Transfer Time-of-Flight mass spectrometer (PTR-ToF-MS) and a chemical ionization mass spectrometer (CIMS) utilizing

iodide ionization (Table S4). A detailed description of the exact species and elemental formulas measured by these instruments, and their associated uncertainties has been described in great detail previously, and in particular as it relates to this flight campaign (*18*). Briefly, the PTR-ToF-MS and CIMS measured a subset of oxygenated species including alcohols, acids, and carbonyl containing compounds, with the PTR-ToF-MS also measuring several hydrocarbons such as aromatics and terpenoid species (full list provided in Hayden et al. 2022). Where an overlapping elemental formula existed between instruments (18 species), the data from the CIMS were retained for subsequent analysis. Calibrations were performed post-flight using gas standard mixtures from Ionicon, Apel-Reimer and Scott-Marrin for 20 compounds for the PTR-MS, and using authentic liquid standards with a liquid calibration unit (LCU; Ionimed Inc.) for the CIMS (25 compounds). Concentrations for additional elemental formulas were derived using sensitivity calculation methods outlined previously for both the PTR-ToF-MS and CIMS (*18*, *48–50*).

Sample Collection and Offline Analysis

Integrated gaseous samples were also collected aboard the aircraft for analysis with offline methods including both VOCs and I/SVOCs. A subset of hydrocarbons was measured after being sampled with passivated, pre-cleaned 1.3L stainless steel canisters (AWAS - Advanced Whole Air Sampler), which were placed in a manifold containing 12 canisters and sampled sequentially (*18*). Canisters were pressurized to ~30 PSI over approximately 15 seconds and were analyzed for relatively lighter gas-phase hydrocarbons (i.e., VOCs not measured from PTR-ToF-MS; C_2–C_{10}). Canisters were analyzed immediately following the flight using analytical instrumentation at the airport consisting of a custom fabricated gas chromatograph (GC) system with cryogenic sample pre-concentration, 2-D gas chromatography, Mass Spectrometric Detection (MS) and Flame Ionization Detection (FID) described in detail previously (*10*, *18*).

Two separate collection systems for adsorbent tubes mounted in wing pods collected time-integrated samples for offline analysis, with the collection systems in the wing pods described in prior work (*35*). Online measurements of flow rate, temperature, and pressure through the adsorbent tubes were also taken aboard the flights, with sampling times ranging from 4-55 minutes at an average flow rate of 292 sccm. To supplement other measurements, the adsorbent tubes focused on collection and measurement of gaseous carbon species in the IVOC/SVOC volatility range. Both adsorbent tube sampling systems were remotely switched on and off to sample along different legs of box flight paths and screen flights near and downwind of OS facilities. One set of tubes (from one wing pod) was packed with Tenax TA absorbent, while the second set of adsorbent tubes (in another wing pod) was packed with a custom blend of quartz wool, glass beads, Tenax TA, and Carbopack X (hereafter denoted QBTX). Both types of sampling tubes in separate wing pods concurrently collected samples for analysis of IVOCs and SVOCs (*51*). Additional details on sorbent packing methods are detailed in previous literature

(*51*). Both types of adsorbent tube samples were integrated across sections of the transect with multiple samples at different altitudes depending on the flight plan (*18*). After each flight, adsorbent tube samples were immediately capped and stored in the dark at -30°C following collection.

Laboratory tests were conducted to verify that minimal analyte breakthrough occurred through QBTX adsorbent tubes. The QBTX tubes were tested at 300 sccm for 15-60 minutes (7% average loss due to breakthrough), with longer sampling times resulting in some loss of C_6–C_9 compounds (13% average loss). This study consequently focused on hydrocarbons and functionalized species C_{10} and larger to ensure that compounds had similar or lower volatility than the breakthrough test analyte sets and similar or greater retention in the QBTX tubes during field sampling (*35*).

Adsorbent tubes containing Tenax TA only were analyzed offline at Environment and Climate Change Canada using GC-EI-MS to characterize ion abundances of collected samples. The Tenax TA tubes were analyzed with a GERSTEL Thermal Desorber and a GC DB-5 MS column (within an Agilent 6890N - MSD Agilent 5973 system), using an n-alkane standard to determine retention times of compounds C_{10} and larger. The column was held initially at 60°C for 3 minutes and then increased to 320°C for 9 minutes. QBTX tubes were analyzed offline using a GERSTEL Thermal Desorber TD 3.5+, and a 6-minute dry purge at 100 mL/min helium flow at 35°C was conducted to remove excess water on the tubes (following GERSTEL methods). The sample was then concentrated on a cold trap maintained at -10 °C before being heated to 325 °C to release adsorbed compounds (*52*). The analytes were then separated on a GC DB-5 MS UI column (Agilent GC 7890B) with helium as the carrier gas. The column was held initially at 35 °C for 5 min before ramping at 10 °C/min to 325 °C and held for 3 min, similar to past work (*35*, *52*). Atmospheric pressure chemical ionization (APCI) and quadrupole time-of-flight mass spectrometry (Agilent 6550 QTOF) were then used to characterize the complex mixture of compounds (collectively referred to as GC-APCI-QTOF). APCI and QTOF parameters are described in past work (*35*, *52*). Analytical standards were also run using QBTX adsorbent tube samples to confirm the identification of the observed hydrocarbons in the mixture using their GC retention times and molecular ions observed via soft ionization (*51*, *52*), including diluted diesel fuel (AccuStandard #2 diesel fuel, DRO-AK-102-LCS-10X-R1), NIST Reference Gulf of Mexico 2779 Macondo Crude Oil, and select oxygen-, nitrogen-, and/or sulfur-containing single analytes (*35*, *51*).

Speciation of complex functionalized mixtures consisted of a targeted search for molecular ions for carbon numbers C_{10}-C_{25} across GC retention time for the C_xH_y compound class (the dominant class present in the oil sands region). Adsorbent tube sampling and analytical conditions were optimized for the molecular weights of this specific carbon number range. C_xH_y ions were grouped into four distinct ring structure groups based on double bond equivalent (DBE):

straight/branched alkanes (DBE 0), cyclic alkanes (DBE 1-3), single ring aromatics (DBE 4-6), and polycyclic aromatic hydrocarbons (PAHs; DBE 7-15) (see Table S5). We note that some fraction of mass associated with single ring aromatics (e.g., DBE 4) may have contributions from multicyclic alkanes (e.g., tetra-cyclic) which are known to exist in OS samples (*32*).

Peaks for C_xH_y ions were extracted at 10 ppm mass tolerance and integrated with custom Igor Pro code. Five-point mass calibrations were conducted across the carbon number and DBE range in our samples using a Macondo Crude Oil reference as the standard following prior work (*52*). Peak areas were then converted to mass using a C_xH_y response factor for individual carbon numbers and DBEs, which was determined based on the known distribution of carbon numbers and DBEs in the crude oil standard with GC and soft ionization (*35*, *52*, *53*). Mass concentrations were calculated from area using sampling volume data for individual tubes. Field blanks employed during sample collection and run on the same GC method were subtracted from flight samples. Known contaminants and artifacts (e.g., those persisting on adsorbent tubes from the adsorbent materials) were also removed.

The QBTX tubes used in this study were optimized for I/SVOC measurements, and employed here to supplement online measurements (e.g., VOCs, OVOCs) from other instrumentation aboard the aircraft (*35*). The adsorbent tube sampling instruments were designed to measure gas-phase compounds. Since the adsorbent tube sampling flow rate into the sampling pod was much lower than its corresponding isokinetic flow rate, particles diverged from the inlet during sampling, resulting in limited particle sampling (*35*). Based on their partitioning coefficients, hydrocarbons below C_{22}-C_{23} were determined to be predominantly in the gas-phase in the atmosphere (*35*), even when using the elevated in-plume organic aerosol concentrations observed in the biomass burning plume (average: 18–22 μg m^{-3}). Thus, the particle-phase contribution to the total observed I/SVOCs in the adsorbent tubes is likely minor at the atmospheric conditions sampled in this work (*35*).

TERRA

The Top-down Emission Rate Retrieval Algorithm (TERRA) was used to estimate hourly mass transfer rates (T_{TC}) from box flight tracks which, when stacked, create a 3D virtual box or 2D screen (Figures 1A, 4B) (*19*). The algorithm uses a mass balance approach that is based upon the Divergence Theorem and has been compared to other aircraft mass balance methods (*21*), and modeled (*54*). Briefly, pollutant concentration data (TC, NO_x and/or NO_y here) from the box flights (and corresponding wind speeds) mentioned above are interpolated using simple kriging, as well as extrapolated from the lowest aircraft altitude to the surface using applicable extrapolation profiles (*19*). Mass transfer rates were derived by integration of the horizontal fluxes into and out of virtual boxes, in units of t h^{-1}, including vertical flux through the box top and the estimated change in mass over the flight time, with the main uncertainty arising from the

extrapolation to the surface. TERRA has been successfully applied to a variety of pollutants (*15*, *16*, *19*, *55*, *56*). Prior to applying TERRA, background TC concentrations were derived as a moving box-car average of data (across a 20 min time window) below the 5th percentile for a given flight and were subtracted from the TC concentration data. This approach has been applied previously for other pollutants (*20*, *29*), and sensitivity analysis has demonstrated that changes in the derived background have little impact on final hourly emissions. TERRA was also used to derive VOC emission rates (Figure S1). VOCs measured from PTR-MS were used directly in TERRA, while VOC data from canisters was correlated with PTR-MS data to derive emissions using a ratio method described in Li et al. (2017) (*15*).

Emission Ratio Determination

TERRA was applied to TC concentrations during box flights to derive hourly emission rates (Fig. S3). These hourly emission rates were used to derive emission ratios relative to NO_x, together with empirical concentration ratios derived from flight data. Emission ratios are expected to be significantly more robust than upscaling hourly emission rates (*29*), and should remain relatively stable at the aggregate facility level despite potential changes in the absolute magnitude of emissions. The concentration density of sub-facility emission sources and nearby atmospheric mixing leads to both combustion and non-combustion sources of TC being mixed and thus moderately correlated ($r^2 \approx 0.4$-0.6) to NO_x in downwind measurements, as indicated in Figure S5. In other studies, anthropogenic tracers are used in similar ways and are often well-correlated across source types downwind of major urban areas, regardless of their specific sources (*57*). This approach has been used previously (*27–29*) and found to reliably compute annual emissions. Annual emissions are determined as,

$$E_{annual} = ER \times E_{NOx,annual}$$

where ER is the estimated emission ratio (of TC to NO_x mass represented as NO_2) for a given facility and $E_{NOx,annual}$ are the NO_x emissions reported annually to inventories (see below). Two approaches to derive emission ratios were applied; the first used the ratio of TERRA-derived TC and NO_x hourly emissions in tonnes hr^{-1} (where suitable flights were available; Table S2), and the second used the correlation ratio of background-subtracted TC and NO_x mixing ratios (i.e., Figure S5). The final ratio used to derive annual TC emissions was estimated as the average (±SD) of both methods (Figure S5; Table S2). The average ratios (±SD) are used because although TC and NO_x are not always co-emitted, their emissions are relatively co-located at the facility-level such that when the aircraft intercepts the oil sands plumes downwind of the sources, the emissions have undergone substantive mixing. In several instances, only single flights around in-situ facilities were conducted, so an average emission ratio from all in-situ operations was employed (53±22 kg TC kg^{-1} NO_x) to derive annual emissions for the 6 measured in-situ facilities (using their individual annual NO_x emissions). We assume that the estimated

annual average ratio is representative within the uncertainty range presented here. The annual emissions were then used to estimate the total measured oil sands TC emissions in Figure 1D.

Use of Emission Inventories

Several emission inventories are utilized in this work, both to scale up hourly to annual emissions (via reported NO_x) and as a comparison to total carbon emissions reported within the oil sands and for other sectors across Canada. NO_x emissions for oil sands facilities were derived from the summation of NO_x data from two sources: Canada's National Pollutant Release Inventory (NPRI) [(25)], which is based upon continuous emission monitoring, emission factors, and/or engineering estimates, and Alberta's Annual Emissions Inventory Reporting Program (AEIR) [(26)]. The NPRI includes stationary and stack sources of NO_x, while off-road NO_x emissions from the various mining activities are provided by the AEIR. Both of these NO_x emissions are reported by the oil sands industry, and combined are found to be in good agreement with satellite-derived estimates of NO_x emissions (*29*). For in-situ facilities, the total inventory NO_x emissions are solely derived from the NPRI.

Facility level TC emissions estimates in this work are compared with the corresponding total VOC reported to the NPRI (i.e., stationary and stack) and AEIR (i.e., mine fleet). The NPRI and AEIR contains both reported VOC emissions for a series of individual species as well as total non-speciated VOC emission estimates. For the year 2018, total VOC reported values were always higher than the sum of reported individual species, and thus were used as the most relevant comparison to measured emissions of TC. The total VOC was converted to carbon mass units for direct comparison to the measured TC emissions, by using the carbon fraction of a C_6 alkane, which was determined as the emissions-weighted average of the speciated VOC reported to NPRI for the same facilities. NPRI-reported emissions for "analytically unresolved hydrocarbon" (0-3×10^{-3} Mt yr^{-1}) were converted to carbon mass units (0-2.6×10^{-3} MtC yr^{-1}) using a calculated carbon mass fraction of 0.87-0.88 based on Tables S2, S6-S7, as it is not explicitly reported by industry.

The sum of annual TC emissions from all measured facilities are compared to the total national VOC reported to Canada's official Air Pollutant Emissions Inventory (APEI) (*30*) for all sectors in 2018 (Figure 1D). VOC emissions are converted to carbon units (tonnes C yr^{-1}) assuming a range of possible carbon molecules, which are represented by the error bars in Fig. 1D. In this case, the bar in Fig. 1D assumes an organic carbon/organic matter (OC/OM) ratio of 0.84 (equivalent to a saturated C_6 hydrocarbon), while the uncertainty bars represent the assumption of a fully-aromatic C_6 compound (i.e., C_6H_6; Benzene, OC/OM = 0.92) and a lightly oxygenated C_6 molecule (i.e., $C_6H_{12}O$; OC/OM = 0.72), which together should adequately bound the true total carbon inventory emissions. The reported reactive organic gas emissions in the South Coast

Air Basin (0.12 Mt yr^{-1}) were also converted to ~0.1 MtC yr^{-1} (potential range of 0.09-0.11 MtC yr^{-1}) based on the range of carbon fraction values above (0.72-0.92).

The results in this work are consistent with underestimates of reported emissions of CO_2, CH_4, and individual VOCs observed in previous work (*15*, *29*, *56*).

Oil Sands Tailings and Laboratory Off-gassing Experiments

During the bitumen extraction process, large volumes of water are added to the oil sands ore to assist in separation of bitumen from the sand and fines, resulting in a fluid tailings "slurry" that is stored in tailings ponds (*58*). Tailings ponds are initially created using overburden from the mine site. As the volume of tailings in the pond grows, coarse tailings are used to build up the sides of the tailings dikes (*59*, *60*). Over time, the solids in the tailings slurry partially settle, resulting in a layer of clarified water at the top of the ponds. This clarified water is pumped back to the processing plant where it is recycled for use in the bitumen extraction process (*59*, *60*).

While tailing ponds can partly separate the solids such that a portion of the water can be recycled back into the extraction process, tailings reclamation and mitigation measures have also been adopted by facilities to reduce the volume of tailings waste stored in ponds (*61*). For comparison, the reported volume of fluid tailings was three times that of bitumen produced from surface mining in 2018 (*23*, *40*). Within these ponds, the dense older layer (known as mature fine tailings or MFT) of fine suspended particles (i.e., sand, silt, clay) with residual bitumen is particularly difficult to separate from wastewater for disposal. Among several methods for dewatering MFT or other fluid tailings (e.g., thickened tailings, non-segregating tailings, composite tailings, fluid tailings centrifugation, permanent aquatic storage structure (PASS), tailings solvent recovery units (TSRU)), atmospheric fines drying was emulated as one method for managing new and legacy tailings waste. In atmospheric fines drying, fluid tailings are mixed with a coagulant and spread over large surface areas to dry over several weeks until subsequent new layers are repeatedly applied, and the remaining solids are ultimately transferred to dedicated disposal areas. While dewatering techniques will expectedly vary, dried tailings are typically left open to the atmosphere for some duration during either processing, temporary storage, or permanent disposal/reuse, and non-fluid tailings represent 40% of total oil sands waste surface area (119 km^2 in 2020) (*43*). Here, MFT off-gassing analysis was conducted across several bench-scale experiments (N=4) with replicate samples collected at various ages (i.e., stages of drying) and environmental conditions.

A 19 L drum of mature fine tailings (MFT) with 0.37 g/mL of total suspended solids was acquired from an industry supplier (Innotech Alberta). The MFT was first agitated to avoid heterogeneity within the sample prior to being subsampled into precleaned analytical bottles and sealed for storage in a laboratory refrigerator. During each test, 1.4 g/L of aluminum potassium

sulfate dodecahydrate (Sigma-Aldrich) was added as a coagulant following industry standards (*62*, *63*). At the start of an experiment, after mixing with alum, the tailings were then transferred to a 3.8 L precleaned closed-system glass vessel, which was filled to a height of approximately 2 inches (volume of 780 mL) similar to industry practices for tailings drying (*64*). A constant flow of zero air (Aadco zero air generator) at 5.0 SLPM (controlled by an Alicat mass flow controller) was used to dry the tailings at atmospherically relevant air exchange rates (e.g., vertical transport velocities) immediately after placement and for time periods ranging from 24 hours up to 9 weeks. For temperature control, the sample vessel was wrapped in aluminum foil and then placed in a dark GC oven (Varian) at a temperature of 25℃ and samples (with replicates) were collected at multiple time points throughout the drying and subsequent aging of tailings. Samples were collected using a ~4 in. 316 stainless steel sampling line at the outlet of the container to exit the oven, with the length minimized and heated to 45°C using a temperature-controlled and insulated heating rope (Omega) to reduce any losses to the transfer tubing material. The temperature of the tailings was monitored using a thermocouple (Omega) fixed to the side of the container as well as a laser temperature reader (Ames Instruments).

For temperature dependent off-gassing experiments, samples were heated to temperatures ranging from 20℃ to 50℃ in the GC oven to simulate a full range of elevated daytime surface temperatures. The effect of irradiance (with a Halogen lamp simulating solar exposure) on emissions was also tested one jar at a time (outside of the oven) using a custom lid outfitted with a quartz glass plate. The full spectrum lamp (OTO E27 Sun Lamp) was placed on top of the quartz plate shining perpendicular to the MFT surface, allowing exposure of the entire surface for 20-minute periods. Irradiation of undried and dried MFT (Figure 5A) occurred 4 hours and 7 weeks after placement in the jar, respectively. To examine the potential enhancement from solar exposure, results were compared across consecutive adsorbent tubes collected across the irradiated and non-irradiated tests, and the laser thermometer (Ames Instruments) was used to confirm the surface remained at ambient temperature. Note that the sensitivity to irradiation shown in Figure 5A, which was independent of temperature, is similar to observations of solar exposure-driven emissions in prior work on asphalt and asphaltene irradiation, including for asphaltene structural features common in the Athabasca region (*65–67*). In addition, the emission factor shown at 11 days in Figure 5A is before crust-breaking occurred. The emission factor after crust-breaking (not shown), which exposed the new surface to further drying, increased by 37%.

Adsorbent tube samples were analyzed using the same Gerstel TD described above and an Agilent HP-5ms GC column (30 m x 250 μm x 1 μm) using the same temperature program as above (i.e., 30°C for initial 5 min hold, 10°C/min ramp to 325°C with 5 min final hold). Average flow and velocity through the column were 1.2 mL/min and 31.1 cm/s, respectively. The initial temperature of the Gerstel TD was ramped up from 30°C at a rate of 400°C/min until it reached a temperature of 310°C where it was held for 6 minutes.

The mass of emissions off-gassing from the MFT in lab experiments was estimated via GC-EI-MS (with adsorbent tube samples) in terms of n-alkane equivalent mass across the volatility range of observed IVOCs-SVOCs (e.g., Figures 5C-D). A five-point calibration curve with three replicates at each concentration was conducted using an n-alkane standard (AccuStandard CT ETPH Alkane Standard, DRH-009S-PAK), spiked on QBTX tubes, and analyzed using GC-EI-MS. The TIC response factor for each compound was derived and averaged to determine the average response factor for a range of relevant IVOC-SVOC compounds in the standard (i.e., C_{12}, C_{14}, C_{16}, C_{18}, C_{20}, C_{22}). Of the n-alkanes used to generate calibration factor, the uncertainty (defined as SD/slope) on the calibration slopes was 6.8% on average (6.3 – 7.6%). The averages of the individual TIC response factors were all within -16% to +25% of the average value used. To delineate I/SVOCs from VOCs, the VOC/IVOC boundary is at $C_{11.5}$, the IVOC/SVOC boundary is at $C_{18.5}$, and the SVOC range ends at $C_{25.5}$ to reflect n-alkane equivalent volatility bins of C_{12}-C_{18} and C_{19}-C_{25} for IVOCs and SVOCs, respectively.

The MFT off-gassing emission factors (Figures 5A-B) were estimated by dividing the background-subtracted total ion response in the I/SVOC range in each sample by the average response factor from the n-alkane standard (above) to determine the measured mass. This mass per sample was then divided by the mass of dry MFT placed in the off-gassing experiment as well as the duration of the sample collection period. Given that only a portion of the 5 SLPM of zero air being flown through the jar was sampled for analysis, the estimated mass was then multiplied by the ratio of the flow rates (i.e., zero air input to sample collection flow) to determine the total mass emitted from the MFT. This emissions factor is in mg n-alkane equivalents emitted per mass of dry MFT per time and the equation can be expressed as:

$$Emission\ Factor\ [\frac{mg}{kg * time}] = \frac{Mass_{emissions\ sampled} * flow\ rate_{zero\ air}}{Mass_{dry\ MFT} * sampling\ period * flow\ rate_{adsorbent\ tube\ sample}}$$

While this laboratory experiment followed available industry practices for atmospheric fines drying (a.k.a. thin lift drying, tailings reduction operations), potential emissions from tailings management industry-wide will be dependent on a range of variables that will expectedly vary across methods and operators, including specific fluid tailings treatment techniques (e.g., equipment used, coagulant type(s), applied layer thickness, re-application frequency), tailings volumes processed, ambient temperatures and solar exposure, coarse tailings management practices and uses, and the transport and disposal of dried tailings. The conditions of the MFT experiments in this study translates to a total potential emission factor ranging from 2 to 4 g I/SVOCs (kg dry MFT)$^{-1}$ (emissions in n-alkane equivalents), considering emissions occurring over a 2 to 4 week period and not including longer-term emissions, elevated temperatures, or solar enhancements. To contextualize the implications of tailings management decisions (assuming these potential emission factors) and demonstrate the need for further research, the magnitude of potential I/SVOC emissions resulting from unmitigated off-gassing from dried fine

fluid tailings across all surface mining oil sands operations is on the order of 10^5 tonnesC yr^{-1} (in n-alkane equivalents). This is based on industry-reported fine fluid tailings processing across surface mining facilities, which is the equivalent of 5-10% of newly-produced tailings volumes and includes a combination of new and legacy tailings (*68*). While only a fraction of MFT currently undergoes drying, the magnitude of potential fluid tailings drying-related emissions emphasizes the need for research on waste management decisions regarding both fine and coarse tailings (new and legacy).

Specifically, the range of potential emissions per mass of dried tailings (i.e., g I/SVOCs (kg dry MFT)$^{-1}$) was estimated using the observed emissions across relevant data points over 2 to 4 week periods in the experiments (i.e., Fig. 5A, Table S7). The industry-wide order of magnitude estimates were calculated using the following equation:

$$Potential\ emissions\ rate\ \left(\frac{tonnesC}{yr}\right) = Potential\ emissions\ factor\ \left(\frac{g}{kg}dry\ MFT\right) * Volume\ dried\ tailings\ produced\ \left(\frac{m^3}{yr}\right) * tailings\ density\ \left(\frac{kg}{m^3}\right) * carbon\ fraction\ \left(\frac{tonnesC}{tonnes}\right)$$

where the potential emissions factor range is the 2-4 g I/SVOCs (kg dry MFT)$^{-1}$ value from above. The total volume of dried (formerly-fine fluid) tailings produced are assumed to be all tailings that achieved "ready to reclaim" (RTR) status reported by each facility (sum = 58 Mm^3 in 2022) (*68*). The range of densities for dry tailings reported volumes is not provided and thus uncertain, but for the purposes of this calculation is taken as the range between an industry-reported value for dried fluid tailings (1450 kg/m^3) (*60*) and packed sand (~1700 kg/m^3). The carbon fraction of oil sands bitumen is 0.84-0.88 gC/g, consistent with flight sample speciation (Fig. 2B) and other calculations in the manuscript (Tables S2, S6-S7) (*33*).

Methods for liquid extract analysis of OS materials

A variety of different samples underwent extraction for analysis via GC-EI-MS (Figure 5C), including unprocessed oil sands, processed oil sands, and tailings (e.g., MFT and its centrifuged components). These samples were extracted and analyzed to evaluate the prevalence of I/SVOC reservoirs in oil sands. The resulting volatility distributions in Figure 5C (solid lines) are thus based on analysis of sample extracts, with comparisons to off-gassing experiments (dotted lines). In addition to fine tailings (i.e., MFT) directly obtained from industry, fluid tailings containing a mix of coarse and fine tailings from the batch extraction of medium-grade oil sands (Innotech Alberta) (*37*), were also analyzed here for comparison.

During sample preparation, bottles containing MFT were first well-shaken to ensure uniformity. 50 mL of the sample was pipetted into 3 separate falcon tubes for phase separation. The falcon tubes were centrifuged for 1 hour at 10,000 rpm (g force = 12300 m/s^2) to separate the bulk solid MFT phase from the aqueous MFT phase and remaining un-settleable particulates (together

represented as "water extract" in Figure 5C). Each supernatant was gently transferred into a 100 mL glass bottle (Boston) and labeled accordingly. While the supernatant was mostly clear, it had a yellow hue with some visible particles that remained suspended following centrifugation. The remaining dark "sludge-like" solids were weighed into round glass bottles and labeled. To examine the total amount of I/SVOCs in the MFT without centrifuging (i.e., phase separation) three samples of well-mixed MFT were directly pipetted into labeled glass bottles. Other samples were similarly prepared without centrifugation. Unprocessed and processed oil sand samples (from industry) were transferred (if solid, sample was weighed) into labeled glass bottles from the primary sample bottle. For the medium-grade coarse and fine tailings sample, free water was separated using cotton fiber filter paper (41 ashless, Whatman), before transferring the solid phase into a labeled glass bottle and sealed.

For the organic extractions, 50-mL of dichloromethane (DCM) was added to all glass bottles containing samples along with magnetic stir bars. The bottles were capped and sealed with a chlorobutyl rubber septum and metal crimp cap. The mixtures were stirred for ~7 days in the dark. After day 7, 1 mL aliquots of the immiscible DCM layer in each sample were removed via syringe through the septum, filtered (0.22 μm PTFE syringe filter), and stored in separate sealed sample vials for subsequent analysis. The DCM extracts were then analyzed by GC-EI-MS via liquid injection (2 μL) using the same Agilent GC-EI-MS (as the MFT off-gassing experiments) with a HP-5ms UI column (30 m x 250 μm x 1 μm) following a 5 min initial hold at 30°C, 10°C/min ramp to 325°C, and a 5 min final hold. Background-subtracted total ion chromatograms were used to show relative volatility distributions (up to C_{28}) in Figure 5C (noting that larger hydrocarbons are expectedly present but outside the observable range here).

Analysis of MFT in separate phases demonstrated that the majority of I/SVOCs were not in the aqueous phase. This is similar to observations with fresh tailings processing in prior work (*37*) that reported ~50 times more residual hydrocarbons in the fine and coarse tailings vs. the water itself.

Supplementary Text

Further description of acyclic vs. cyclic alkane observations (Figure 2 ratios)

Both GC-TOF and GC-EI-MS measurements via aircraft reveal relatively minor contributions from acyclic (i.e., linear/branched) alkanes (Figures 2B-D). This is atypical of observations of common I/SVOC sources such as diesel fuel combustion, which has a cyclic-to-acyclic alkane ratio close to ~1:1 (*7*). The observed cyclic-to-acyclic alkane mass fragment ratios in GC-EI-MS data (i.e., m/z 55/57) (*34*) are consistently high across flights (Figure 2D) with an average of 2.0±0.1 for surface mining facilities and 1.9±0.2 for in-situ facilities in the summertime, and

1.7±0.1 in the springtime (surface mining only). The prevalence of cyclic alkanes (relative to acyclic alkanes) is also evident in the unit-resolution EI-MS mass spectra across the SVOC range, similar to that of oil sands materials obtained from the oil sands industry (i.e., unprocessed, processed, waste; Figure 2C), where both spectra have prominent mass-to-charge (m/z) fragments associated with mono- and multi-cyclic alkanes (e.g., m/z 69, 81, 83, 95, 109, 123) (Figure 2C) (*34*). These observations are consistent with prior work showing that the composition of Athabasca bitumen is depleted of acyclic alkanes and characterized by a large fraction of mono- through tetra-cyclic alkanes in the ~C15–C23 range (*32*). In all, cyclic-to-acyclic alkane ratios are elevated across flights and oil sands materials, and dissimilar to that of I/SVOC emissions from other traditional sources (i.e., diesel combustion). These mass spectral observations further support that the ambient I/SVOC species from adsorbent tube samples are oil sands-derived.

Additional description of Flights 25, 26, and 29

Flight 25 and Flight 26 sampled two boreal wildfire smoke plumes originating near Lac La Loche in northern Saskatchewan, Canada on 25 June 2018 (Figure 3A, 3B). The aircraft flew the same straight-line tracks at multiple altitudes through the smoke plumes in each of the transects, intercepting the plumes at each of five downwind locations (*18*, *35*). Concentrations across the IVOC-SVOC volatility range (measured via Tenax tubes with GC-EI-MS) were relatively low in all Flight 25 samples across the first 4 screens, and even lower in samples taken along screen edges. Immediately following Flight 25, Flight 26 collected four samples along screen 5 at multiple altitudes (Figure 3B) to intercept the forest fire plume downwind of a collection of major surface mining oil sands facilities.

Flight 29 was conducted on 4 July 2018. Similar to the above methodology, the aircraft flew along screens 1-4 consisting of straight-line tracks at different altitudes downwind of surface oil sands facilities, but in the absence of any forest fire plume. As described in the main text, screen 4 was sampled downwind of in-situ extraction sites (Figures 3D, 4C). While the underlying on-site sources and emission pathways contributing to emissions from this and other in-situ facilities are unclear, we note that prior work has reported suspended solids levels of 30-290 mg/L in in-situ waste streams (*69*), though their treatment and disposal practices are uncertain and not publicly disclosed.

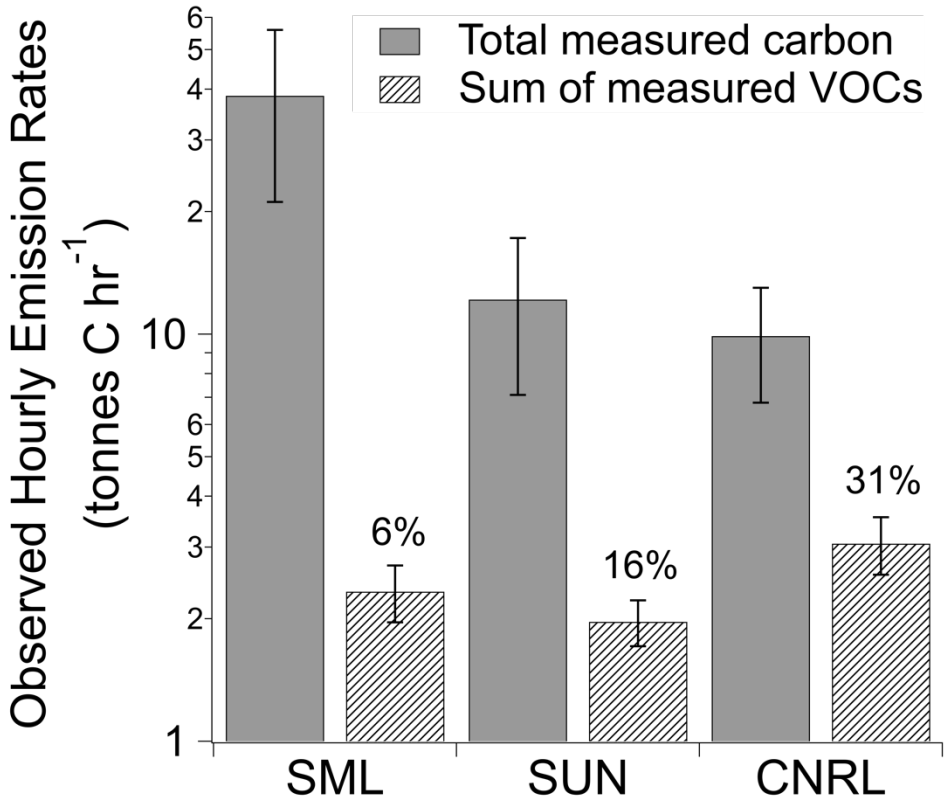

Fig. S1. Measured VOCs only account for a fraction of total measured organic carbon above major OS facilities. Hourly measured emission rates of total organic carbon from the flights are compared to the summed hourly emission rates for the measured VOCs from both PTR-MS and whole-air samples together (converted to carbon units). The percent contribution of the sum of VOCs to total measured carbon is labeled for each major facility. Error bars reflect the standard deviation across flights and the propagated uncertainty from TERRA.

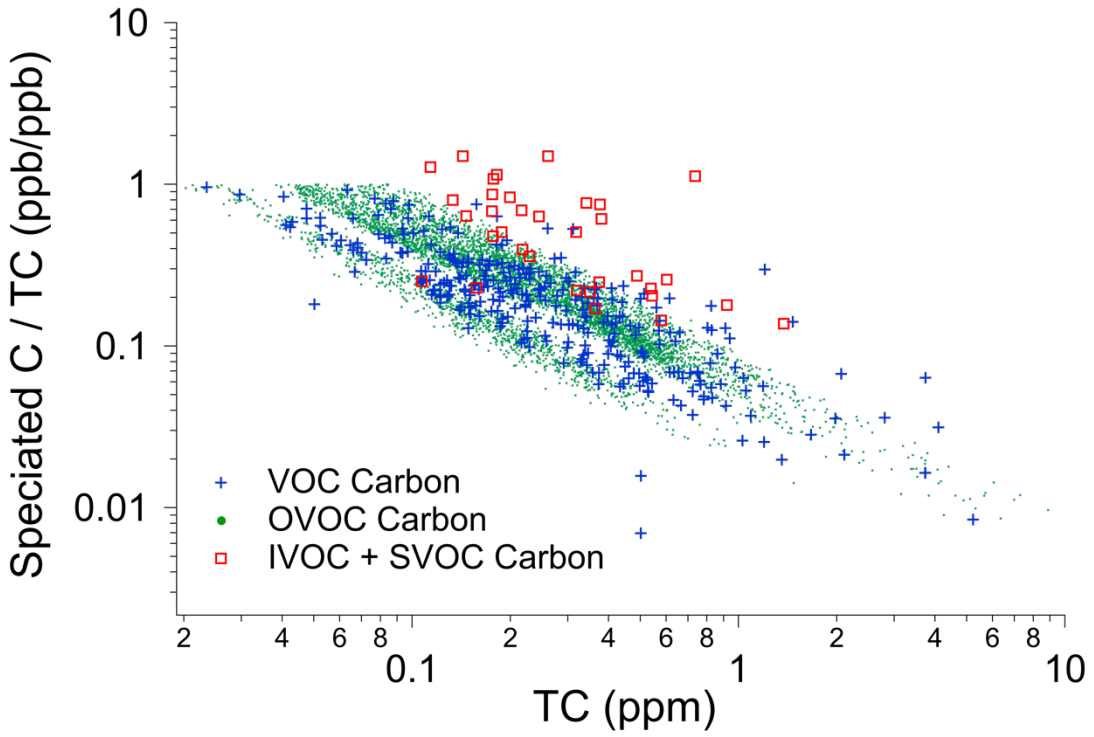

Fig. S2. Relative contributions to total observed carbon. The fraction of speciated carbon attributed to VOCs, OVOCs, and IVOCs + SVOCs is shown compared to TC measurements. I/SVOCs often make up a significant fraction of total measured carbon, and VOCs+OVOCs explain a decreasing fraction in the most concentrated plumes (i.e., concentrations above the 75th percentile of all total carbon).

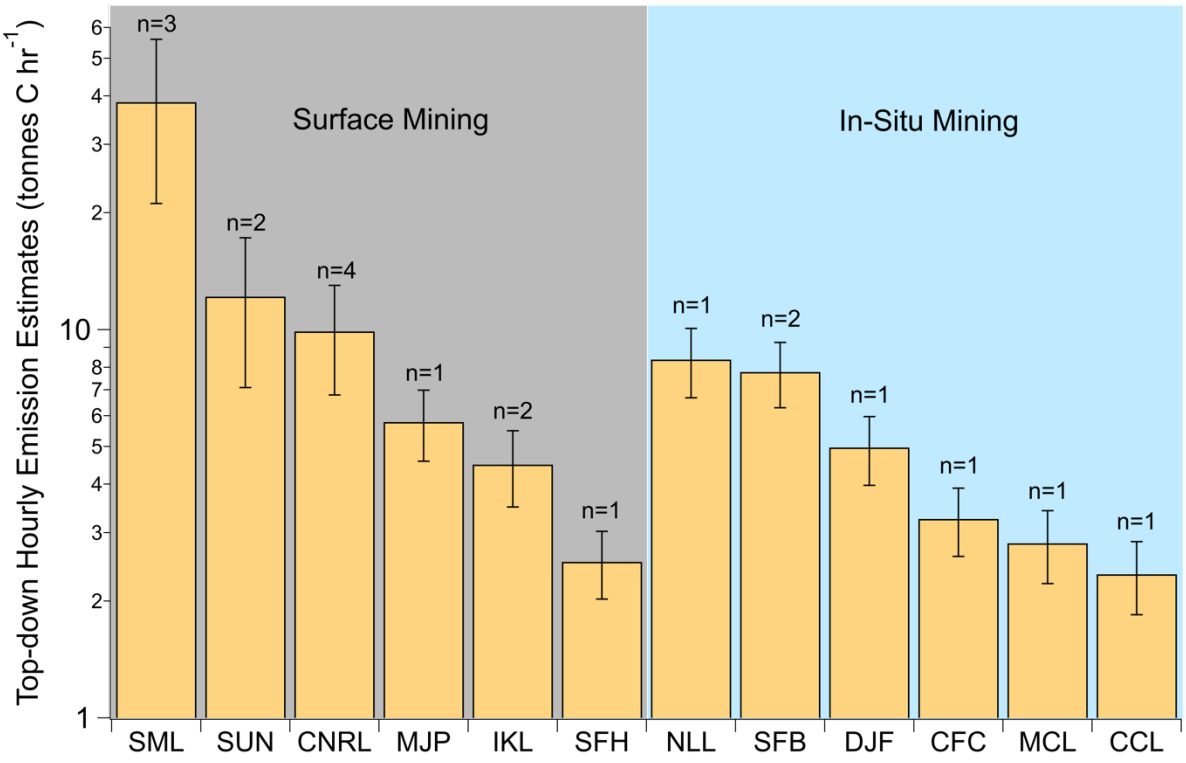

Fig. S3. Hourly emissions of TC derived with TERRA from all flights around surface and in-situ OS facilities (see Table S2). For many of the in-situ facilities, there was only one flight (i.e., N=1). Error bars represent the standard deviation of flight results (except where N=1, which in that case is the uncertainty associated with the hourly TERRA values).

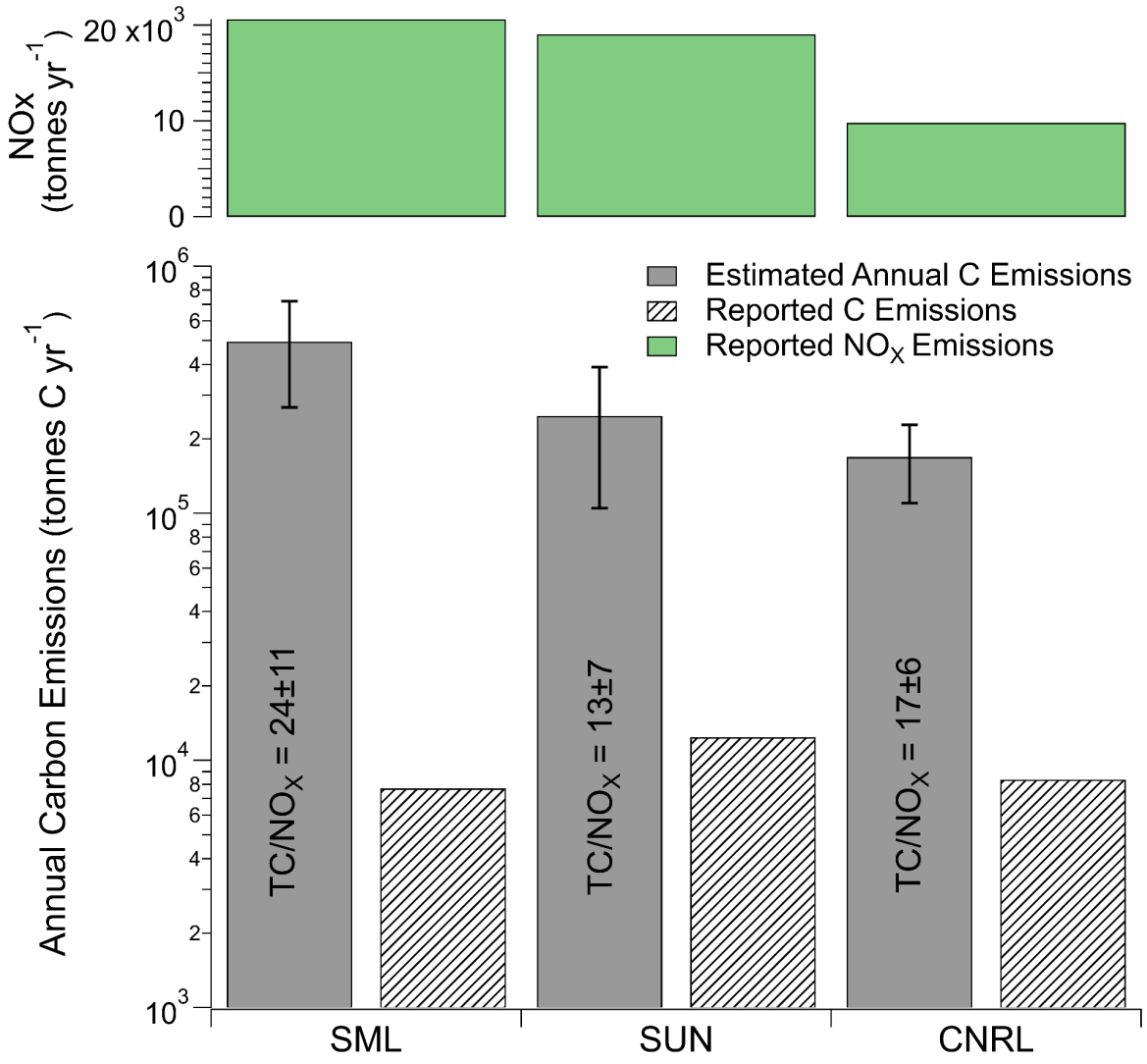

Fig. S4. Comparison of annual carbon emissions to reported carbon emissions along with measured TC/NO_x ratios. The reported carbon emissions are from NPRI and AEIR Facility-Reported Data (Table S2). The measured TC/NO_x ratios were derived using both TERRA emissions and the correlation of background-subtracted TC and NO_x. The TC/NO_x ratio is used with the reported NO_x emissions from each of the facilities to determine the solid grey bars (i.e., TC/NO_x × $NO_{x,\,reported}$ = TC). The annual reported NO_x emissions used are shown in green, which includes both NPRI and AEIR added together. Estimated annual carbon emissions are scaled using NOx reported inventories (see above section on emission ratio determination).

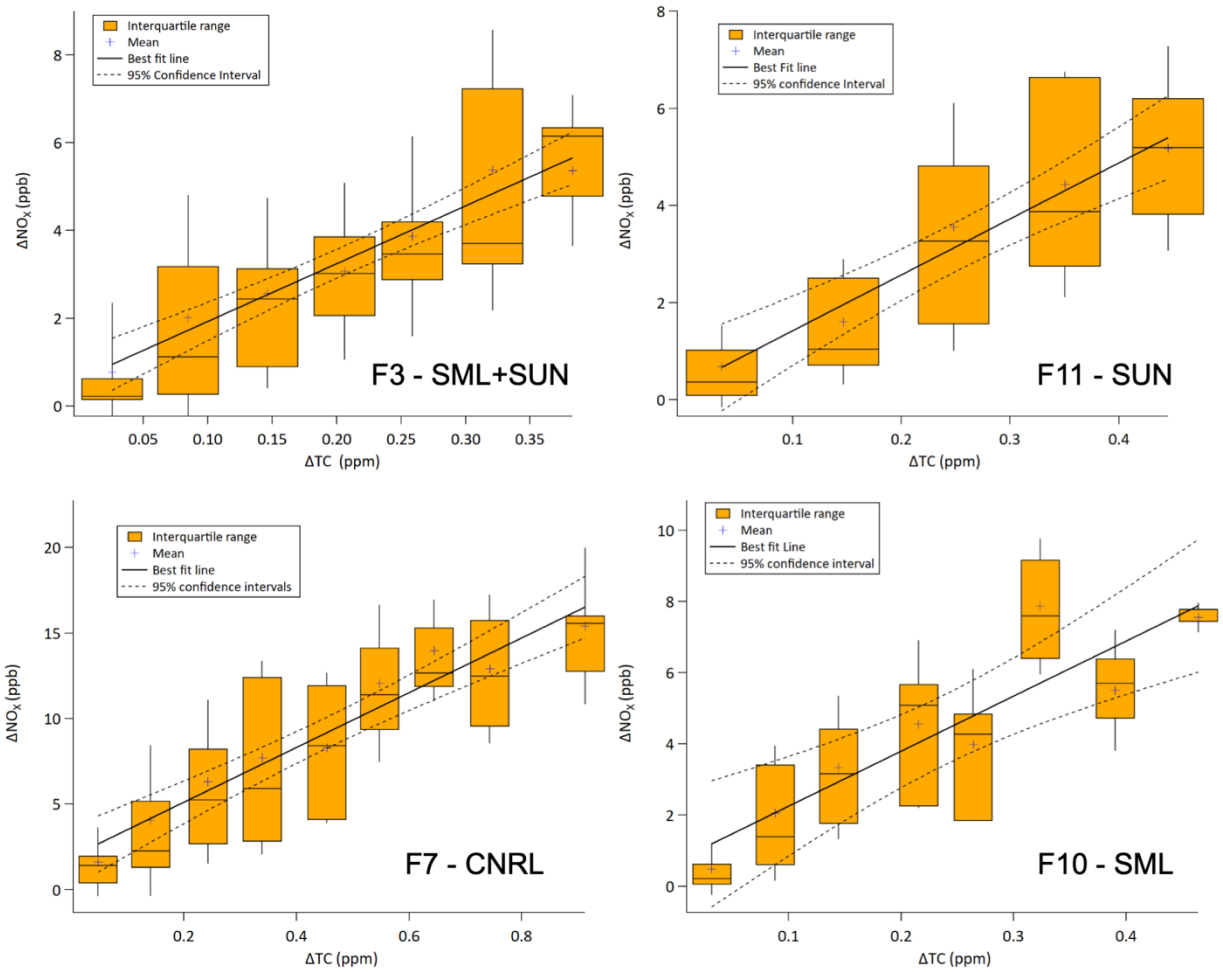

Fig. S5. Examples of empirical correlation emission ratios for surface mining operations. Mixing ratios of TC and NOx have been background subtracted as described above (see section on emission ratio determination). Interquartile range reflects both combustion and non-combustion sources of TC.

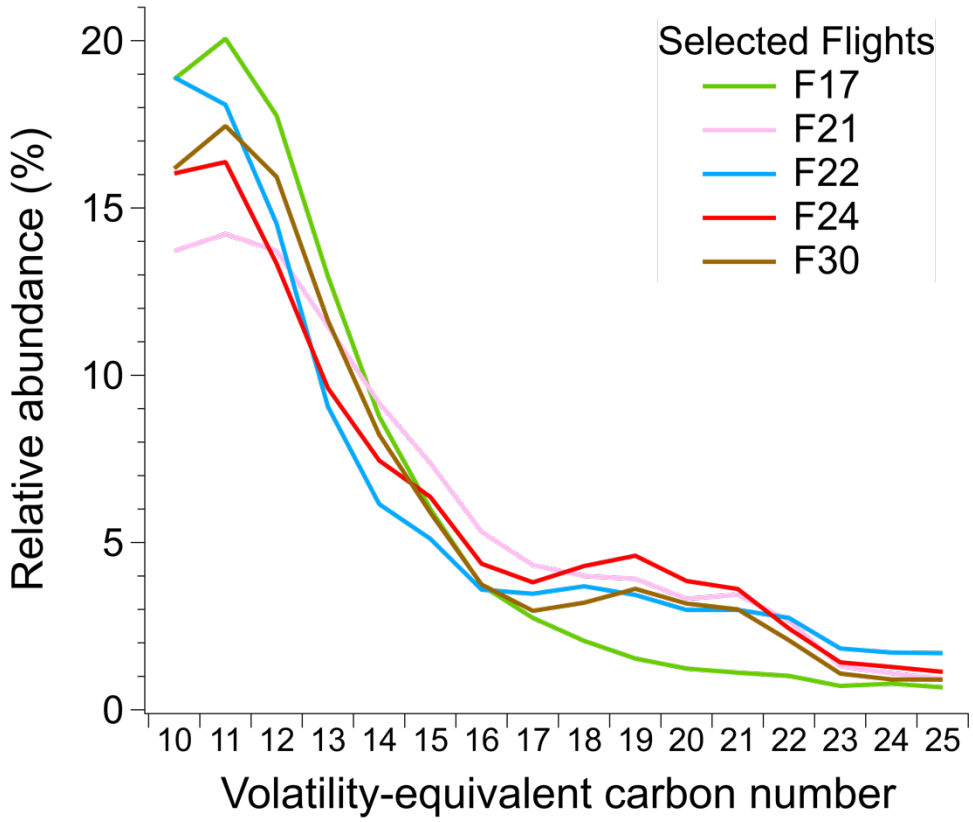

Fig. S6. Binned GC-EIMS chromatograms for other flights not shown in Figure 2A. Chromatograms for samples (Tenax TA sorbent tubes) on additional flights taken in areas not adjacent to facilities, but within the oil sands producing region, show lower relative signal in the range of larger IVOCs and SVOCs. Still, samples are likely to have some influence from oil sands facilities in the region.

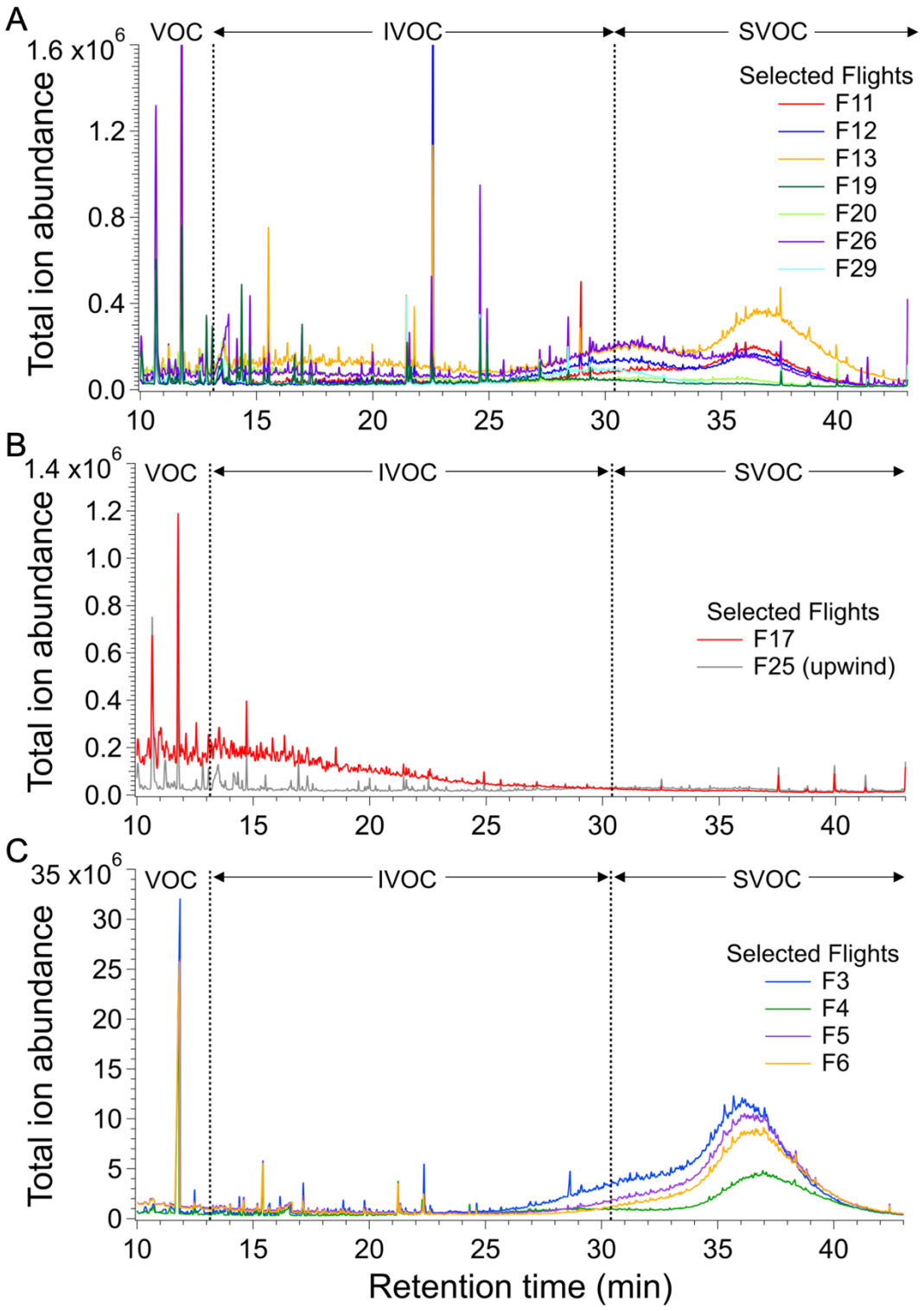

Fig. S7. Total Ion Chromatograms (TIC) across selected flight samples (Tenax TA sorbent tubes). GC-EI-MS chromatograms are provided for A) the same summertime flights that are binned by volatility in Figure 2A, B) samples on flights in areas not adjacent to oil sands

facilities (with relatively lower abundances in the I/SVOC ranges compared to other flight samples), and C) springtime flight samples that show pronounced unresolved complex mixtures in the I/SVOC ranges, similar to those in summertime flights. The VOC/IVOC boundary is shown at $C_{11.5}$, the IVOC/SVOC boundary is shown at $C_{18.5}$, and the SVOC range ends at $C_{25.5}$ to reflect n-alkane volatility equivalent bins of C_{12}-C_{18} and C_{19}-C_{25} for IVOCs and SVOCs, respectively.

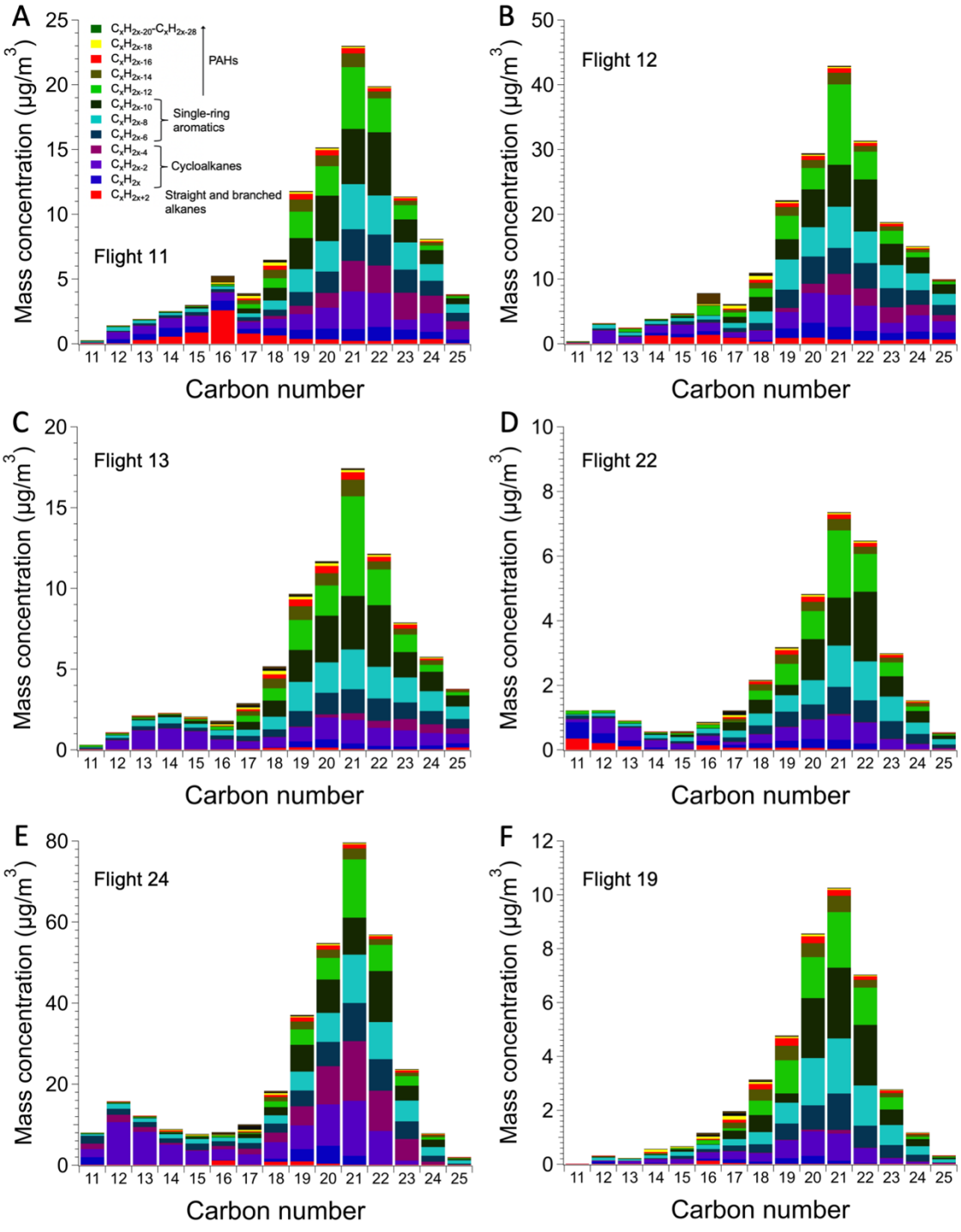

Fig. S8. Additional example of GC-TOF mass distributions of individual flight samples (QBTX sorbent tubes) with SVOC and aromatic content. Panels A-F show detailed chemical composition of hydrocarbons in samples from selected flights to supplement the average shown in Figure 2B, which is also similar to the EI-MS data showing a peak contribution in C_{19}-C_{23}

species across flights in Figure 2A. Average altitudes for samples in A-F are 750 m, 1052 m, 949 m, 796 m, 781 m, and 908 m, respectively. Carbon number distributions vary between flights and show prominent SVOC mass concentrations and significant aromatic content. The legend gives the breakdown of molecular structures for each carbon number bin, ranging from acyclic alkanes to PAHs.

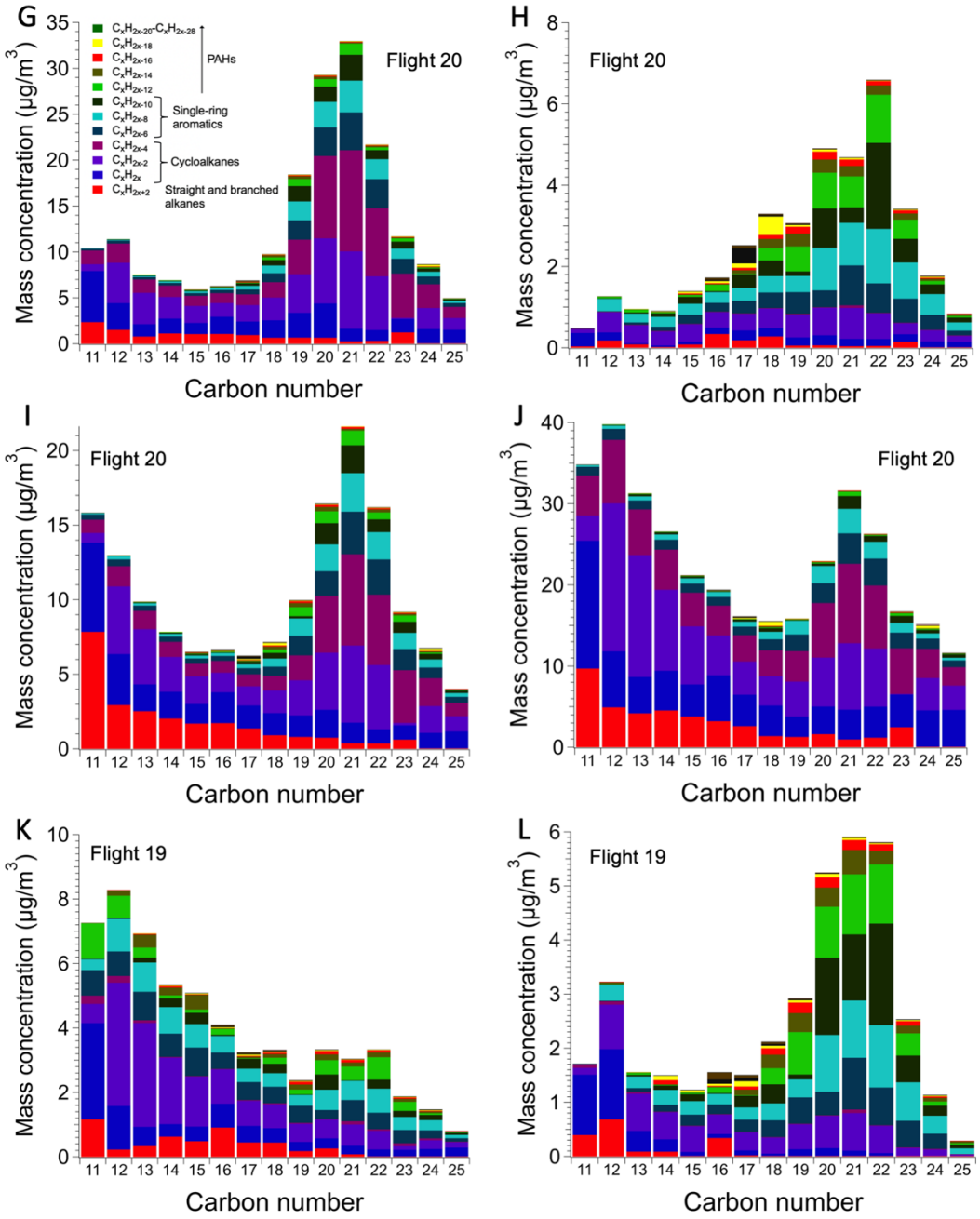

Fig. S9. Additional examples of GC-TOF mass distributions of flight samples (QBTX sorbent tubes) with greater IVOC content. Panels G-L show detailed chemical composition of hydrocarbons in samples from Flights 19 and 20. Average altitudes for samples in G-L are 661 m, 950 m, 1176 m, 640 m, 519 m, and 792 m, respectively. Volatility distributions show a mix of both IVOC (C_{12}-C_{18}) and SVOC presence with prevalent but varying amounts of cycloalkanes.

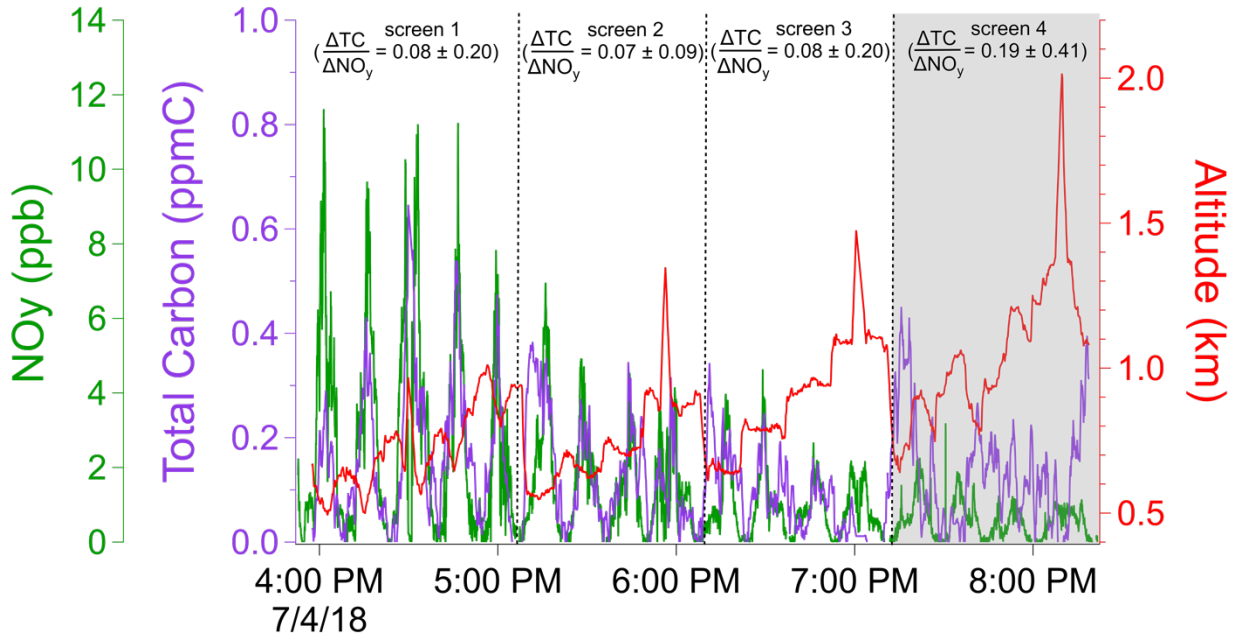

Fig. S10. Supplement to Fig. 4A. TC and NO_y mixing ratios with altitude for Flight 29.

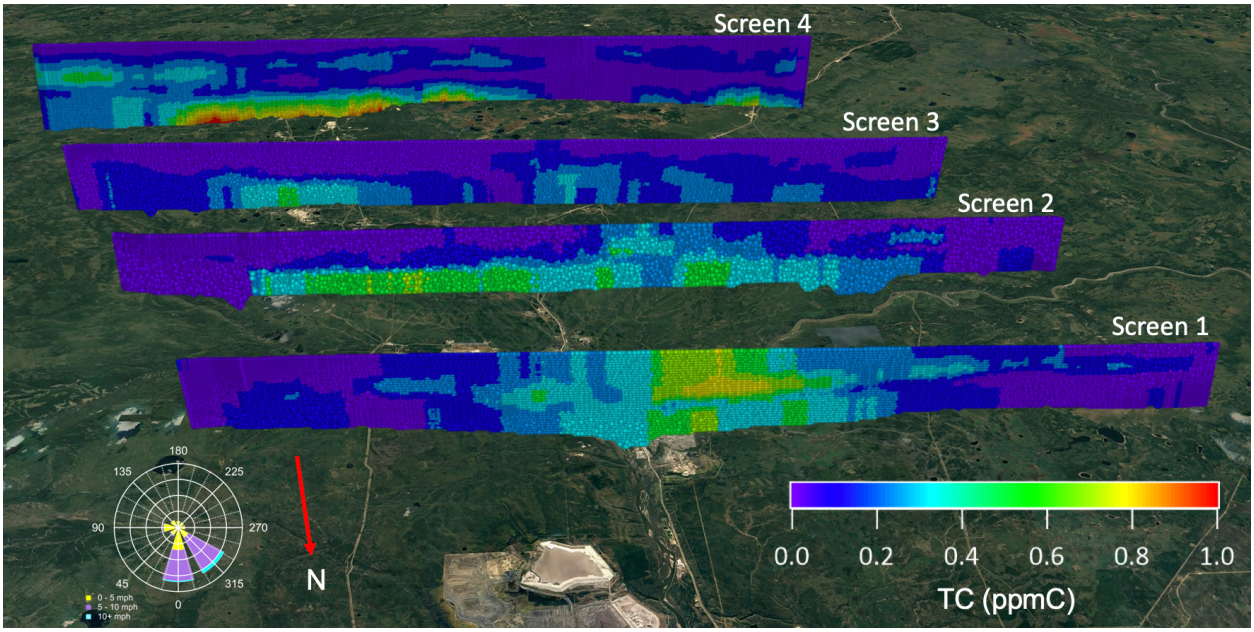

Fig. S11. Elevated TC concentrations in Flight 29. 2-dimensional virtual screens (generated by TERRA) with a wind rose for all 4 flight tracks in F29 downwind of surface mining facilities (screens 1-3) and in-situ mining sites (screen 4).

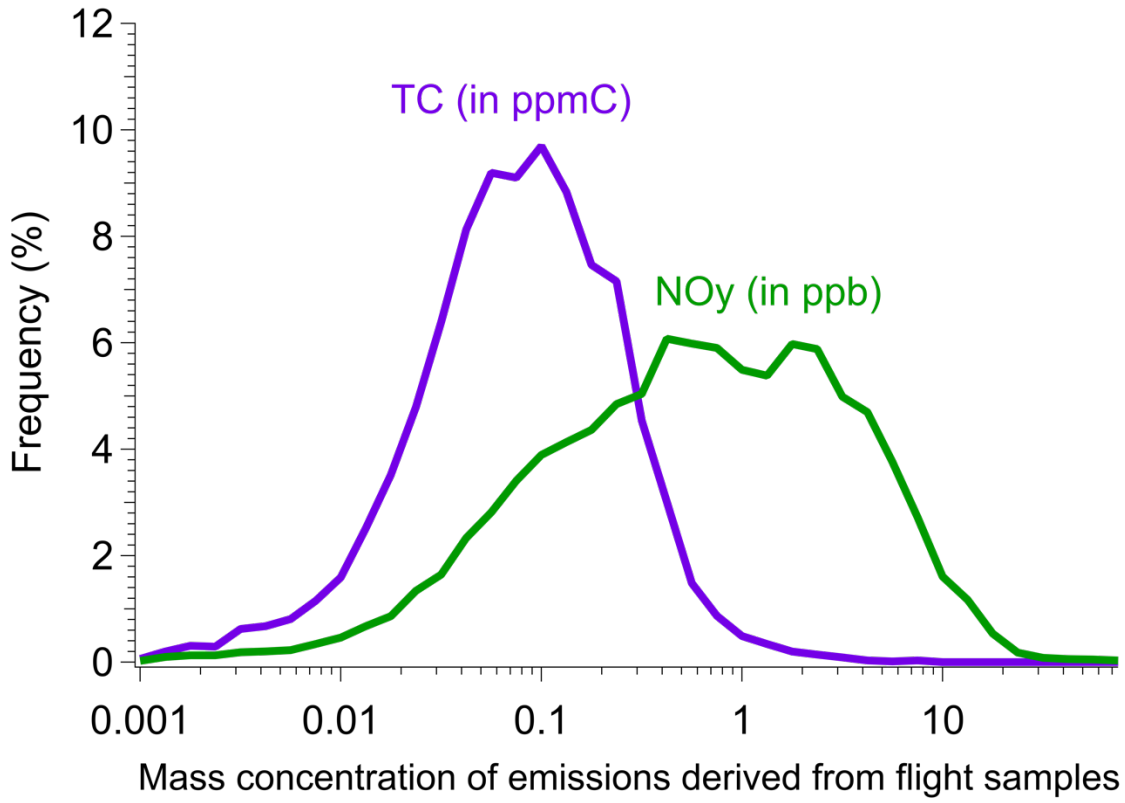

Fig. S12. Frequency distribution of TC and NO_y mixing ratios across all flights. For reference, TC mixing ratios (in ppmC) for the 10^{th}, 20^{th}, 25^{th}, 50^{th}, and 75^{th} percentiles are 0.008, 0.023, 0.031, 0.072, and 0.159, respectively.

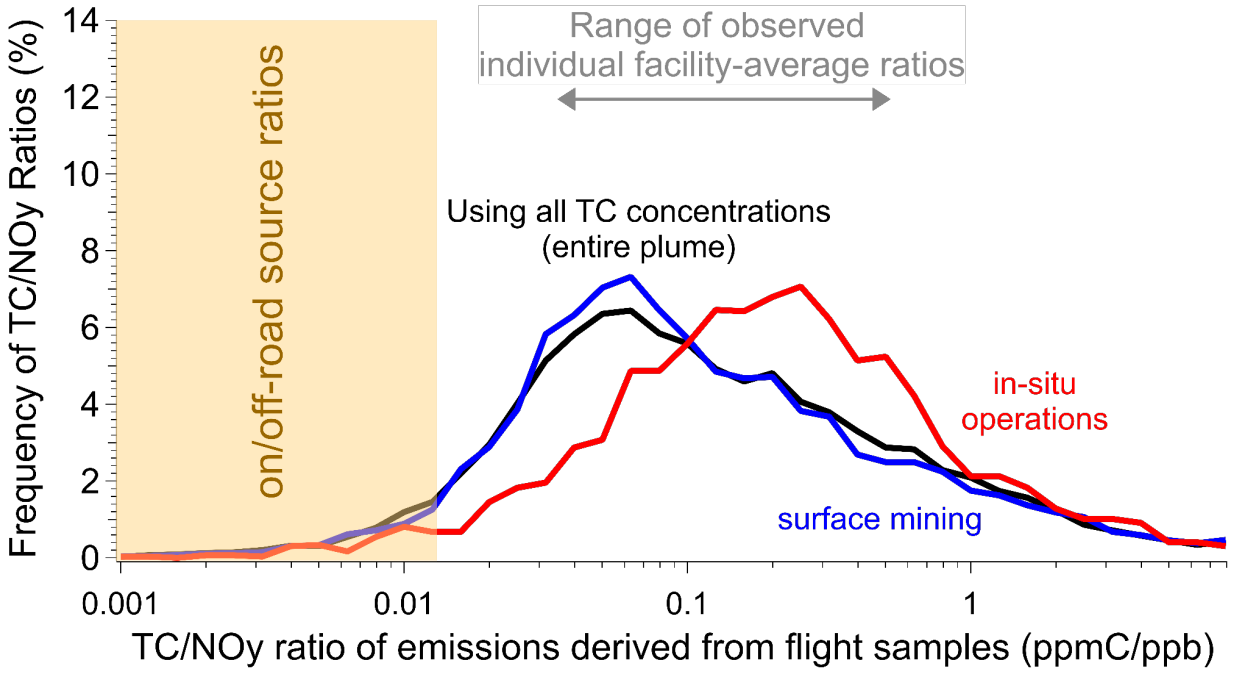

Fig. S13. Supplement to Fig. 4C. Frequency distribution of TC/NO_y ratios across all flights using all TC concentrations (not just the top 50th percentile of data as in Fig. 4C) across all flights (black line), in-situ only flights, and surface mining only flights. Note that in Fig. 4C, the ratios were calculated using TC concentrations above the 50th percentile within each data subset to focus the analysis on more concentrated plumes and reduce potential bias from lower concentration "background" data, while still including diluted plumes further away from sources. The in-situ TC/NO_y ratios for the top 50% of in-situ facility plumes are likely shifted towards higher ratios than those for surface mining given the reduced presence of combustion-related NO_y sources (e.g., off-road equipment/vehicles) compared to surface operations and the limited correlation between TC and NO_y around in-situ sources (e.g., Figure 4A, screen 4). For comparison, the distribution using all concentrations is shown in Fig. S12 and here.

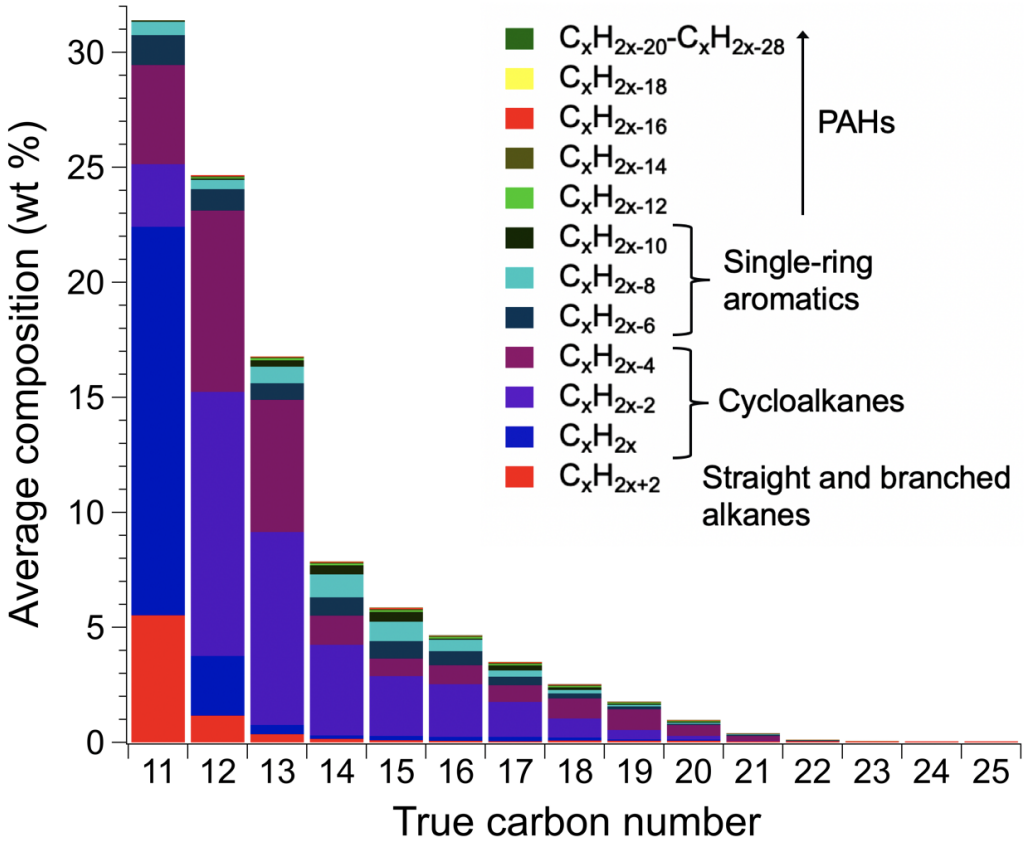

Fig. S14. Supplement to Fig. 5D. Average chemical composition of off-gassing from fresh and partially-dried MFT samples that were not exposed to irradiation, via APCI-MS (see Table S10).

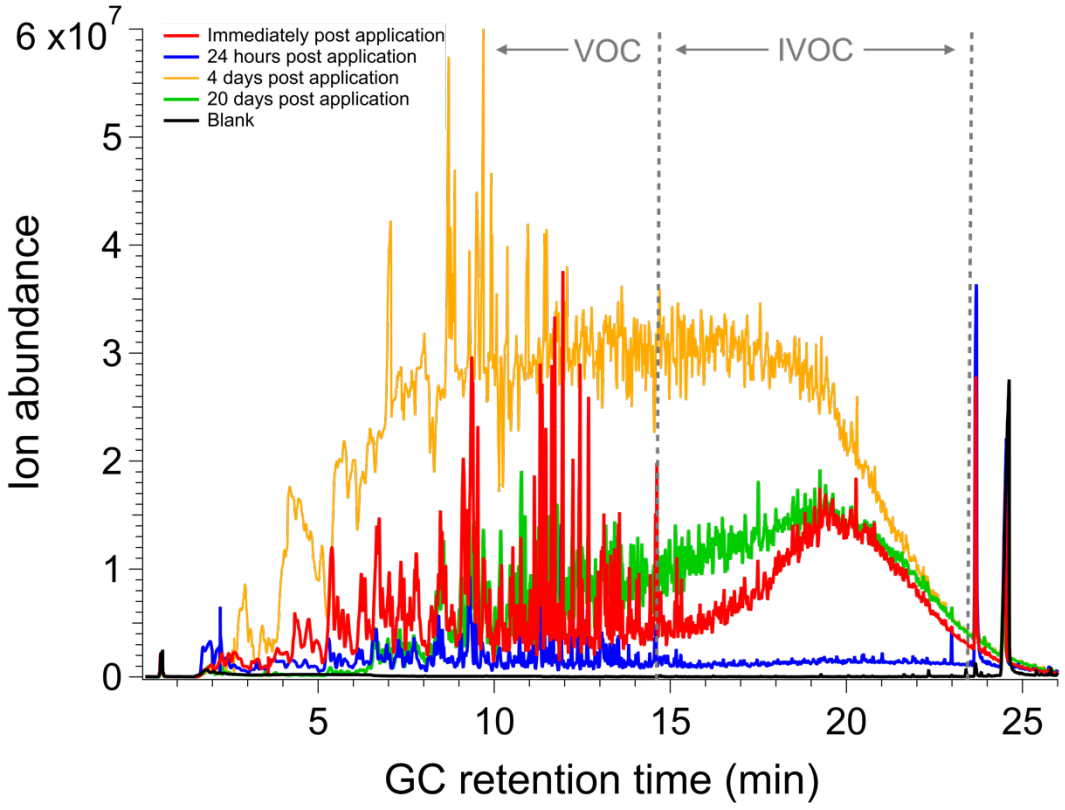

Fig. S15. GC-EI-MS analysis of off-gassing emissions from mature fine tailings (MFT). Total ion chromatograms from initial off-gassing emissions include a range of VOCs to SVOCs (red). Emissions decrease promptly after "application" (blue) and increase markedly as the surface of tailings dries and the water barrier is removed (yellow, at 4 days here). Emissions remain elevated after tailings dry, with 20 days (green) shown here. Frequent standards were run to ensure that the instrument detector response did not substantially change across the sample analysis period.

Table S1. Flight information for studied facilities.

Flight #	Facilities studied	Take-off (GMT)	Landing (GMT)	Mean wind speed (m/s)	Transect altitude range (m ASL)[1]	Approx. boundary layer height (m ASL)[2]
3	Nexen Long Lake	4/9/18 17:55	4/9/18 23:15	4.9 ± 1.6	600 - 1500	2000
4	CNRL Horizon, Imperial Kearl, Suncor Firebag	4/10/18 17:40	4/10/18 21:54	5.5 ± 1.9	400 - 1400	1350
7	CNRL Horizon	5/30/18 16:28	5/30/18 19:03	2.4 ± 1.0	400 - 1480	1600
8	CNRL Horizon, Suncor Fort Hills	5/31/18 16:42	5/31/18 21:42	2.3 ± 1.5	430 - 1600	1700
9	Suncor Firebag, Suncor Millennium	6/1/18 20:40	6/2/18 0:30	6.5 ± 1.5	500 - 1450	1550
10	Syncrude ML	6/6/18 16:46	6/6/18 19:28	4.4 ± 1.5	500 - 1450	1450
11	Suncor Millennium	6/6/18 20:53	6/6/18 23:37	4.2 ± 1.8	400 - 1500	1700
12	Devon Jackfish, MEG Christina Lake, Cenovus Christina Lake	6/7/18 15:05	6/7/18 19:20	7.5 ± 2.3	700 - 1400	1675
13	CNRL Muskeg River	6/7/18 20:25	6/7/18 23:05	4.2 ± 1.9	450 - 1550	1750
17	CNRL Horizon	6/15/18 16:33	6/15/18 21:15	2.8 ± 1.4	430 - 1700	2100
18	Cenovus Foster Creeke	6/16/18 14:55	6/16/18 19:43	2.9 ± 1.6	850 - 1650	2000
19	Syncrude ML	6/18/18 14:54	6/18/18 18:41	3.6 ± 1.8	400 - 1000	1800
20	Syncrude ML	6/19/18 14:50	6/19/18 19:17	4.3 ± 1.6	450 - 1100	>1800
21	Imperial Kearl	6/20/18 14:51	6/20/18 18:37	4.2 ± 1.5	400 - 800	>1600
22	Transformation flight, 4 screens, following plume of Syncrude ML	6/21/18 14:52	6/21/18 19:16	3.6 ± 1.8	450-1000	1200
24	Transformation flight, 3 screens, following plume from all facilities	6/24/18 14:49	6/24/18 19:15	5.8 ± 1.8	600-1400	1350
25	Transformation flight, 3 screens, following forest fire plume before the facilities	6/25/18 14:45	6/25/18 19:16	7.9 ± 2.4	600-1400	1300
29	Transformation flight, 4 screens, following plume from all facilities	7/4/18 15:46	7/4/18 20:33	6.3 ± 2.0	450-1000	1300
30	Transformation flight, 3 screens, following plume from all facilities	7/5/18 14:57	7/5/18 19:35	7.0 ± 1.8	450-1000	1500

[1]The range of altitude transects ASL (above sea level) are spaced by approx. 100 m each, ±50 m.

[2]The boundary layer is estimated based on the temperature vertical profile measured from the aircraft. The top of the boundary layer was assumed when the layer abruptly dropped (along with various pollutant concentrations such as NO_x), so the uncertainty in the layer height may be ±100 m. The aircraft was always flown above the boundary layer for each flight, so the exact top of the layer is not as important.

Table S2.* Emission rates based on TERRA, 2018 National Pollutant Release Inventory (NPRI) and AEIR Facility-Reported Data, and production rates based on Alberta ST39 (*23*) **and ST53** (*31*) **for each of the OS facilities investigated.** Hourly TC emissions and TC/NO_x ratios represent average across flights when N>1 or include a conservative 50% uncertainty where only 1 flight was conducted. Number of flights used for each TC emission estimate is shown in Figure S3.

Facility Name	Acronym	Facility Type	Flights that Sampled this Facility	Average Measured TC Emissions (tonnes C hr^{-1})	Average Measured Hourly NOx (as NO_2) Emissions (TERRA; tonnes hr^{-1})	Annual Total Crude Bitumen Production (m^3)[a,h]	Estimated Annual TC Emissions (Mt C)[b]	Average Emission Ratio TC/NOx (ER; kg C kg^{-1} NOx)	Annual Reported NOx (as NO_2) Emissions (kt yr^{-1})[c]	Annual Reported TC Emissions (tonnes C yr^{-1})[c]	Emissions per Average Crude Bitumen Production (tonnes C m^{-3} crude bitumen) (estimated % production by mass)[g,h]
Syncrude Mildred Lake	SML	Surface mines	F10, F19, F20	38.5±17 (27.7-58.6)	2.4±0.9	6,865,642	0.5±0.2	24±11	20.62	7704	0.044-0.10 (5.2-12%)
Suncor	SUN	Surface mines	F9, F11	12.2±5 (8.6-15.8)	1.6±0.3	15,010,601	0.25±0.14	13±7	19.05	12410	0.007-0.026 (0.87-3.1%)
Canadian Natural Resources Ltd	CNRL	Surface mines	F4, F7, F8, F17	9.9±3.1 (6.0-13.1)	0.8±0.4	15,311,908	0.17±0.06	17±6	9.82	8356	0.007-0.015 (0.85-1.8%)
CNRL Muskeg River/Jack Pine	MJP	Surface mines	F13	5.8±1.2	NA	17,103,097	NA	NA	8.44	4191	NA
Imperial Kearl Lake	IKL	Surface mines	F4, F21	4.5±1.0 (3.9-5.2)	0.35	12,920,362	0.11±0.05	22±10	5.04	3238	0.005-0.012 (0.55-1.5%)
Fort Hills	SFH	Surface mines	F8	2.5±0.5	0.28	7,534,498	0.065±0.03	15±8	4.3	842	0.005-0.013 (0.55-1.5%)

Suncor Firebag	SFB	In-situ	F4, F9	7.8±1.5 (6.7-8.8)	0.15±0.05	11,681,490	0.15±0.06	60±30	2.89	267	0.008-0.018 (0.91-2.1%)
Devon Jack Fish	DJF	In-situ	F12	5.0±1	0.06±0.012	5,730,017	0.05±0.02	79±39.5	0.99[d]	160	0.005-0.012 (0.62-1.5%)
Cenovus Foster Creek	CFC	In-situ	F18	3.3±0.7	0.09±0.02	9,265,544	0.09±0.04	35±18	1.74[e]	184	0.005-0.014 (0.64-1.7%)
MEG Christina Lake	MCL	In-situ	F12	2.9±0.6	0.08±0.016	4,440,627	0.05±0.02	33±17	0.92[f]	120	0.007-0.016 (0.80-1.9%)
Cenovus Christina Lake	CCL	In-situ	F12	2.3±0.5	0.04±0.01	11,515,011	0.06±0.03	65±33	1.16	203	0.003-0.008 (0.31-0.93%)
Nexen Long Lake	NLL	In-situ	F3	8.4±1.7	0.26±0.05	2,540,607	0.09±0.04	32±16	1.67	128	0.020-0.051 (2.3-6.1%)
							In-situ Average Emission Ratio	53±22			

[*]Note: Each box around the facility takes about 1-2 hours depending on the size of the box around a given facility. Time of day is between 12-6 pm depending on the establishment of the boundary layer each day, which was decided based on air quality model forecasts done at the time.

[a]From Alberta Mineable Oil Sands Plant Statistics (ST39) and Alberta In Situ Oil Sands Production Statistical Report (ST53).

[b]In-situ emissions are calculated based on the average of all in-situ flights (since only one flight was flown per facility).

[c]From NPRI and AEIR Facility-Reported Data, converted to carbon units using emissions-weighted average of the speciated VOC reported for the same facilities.

[d]Sum of the three Jackfish plants (JKF1, JKF2, JKF3) which are reported separately.

[e]Includes the Caribou North Compressor Station.

[f]Includes the MEG cogeneration facility.

[g]Using the carbon fraction = 0.84 gC/g bitumen, calculated from He et al., 2013 (*33*). Measured emissions were scaled annually for this calculation. The range of emissions per production and the associated percentages are derived from the propagated standard deviation from the emission estimates and the variations in monthly bitumen production. Note: crude bitumen production is not a direct predictor of TC emissions as they are not correlated here (r = 0.33 for surface mining and r = 0.45 for in-situ facilities).

[h]We include only crude bitumen production excluding facility receipts to avoid double-counting across facilities. Including receipts, SML annual production would be 17,501,672 m^3 and 2.0-4.7% hydrocarbon emissions intensity, and Suncor annual production would be 36,071,653 m^3 and 0.4-1.3% hydrocarbon emissions intensity.

Table S3. Required reported VOCs and other reactive organic species in the National Pollutant Release Inventory (NPRI). Categories are named by the NPRI (*70*)**.**

Part 1: Group A Substances	Acetaldehyde, Acetonitrile, Acetophenone, Acrolein, Acrylamide, Acrylic acid , Allyl alcohol, Aniline , Benzene, Benzoyl chloride, Benzoyl peroxide, Benzyl chloride, Biphenyl, Bis(2-ethylhexyl) adipate, Bis(2-ethylhexyl) phthalate, Bromomethane, 1,3-Butadiene, 2-Butoxyethanol, Butyl acrylate, i-Butyl alcohol, n-Butyl alcohol, sec-Butyl alcohol, tert-Butyl alcohol, Butyl benzyl phthalate, 1,2-Butylene oxide, Butyraldehyde, Carbon disulphide, Carbon tetrachloride, Carbonyl sulphide, Catechol, CFC-11, CFC-12, CFC-13, CFC-114, CFC-115, Chloroacetic acid , Chlorobenzene, Chloroethane, Chloroform, Chloromethane, Cresol (all isomers, and their salts), Cumene, Cumene hydroperoxide, Cyclohexane, Cyclohexanol, Decabromodiphenyl oxide, 2,6-Di-t-butyl-4-methylphenol, Dibutyl phthalate, o-Dichlorobenzene, p-Dichlorobenzene, 3,3′-Dichlorobenzidine dihydrochloride, 1,2-Dichloroethane, Dichloromethane, 2,4-Dichlorophenol , 1,2-Dichloropropane, Dicyclopentadiene, Diethanolamine , Diethyl phthalate, Diethyl sulphate, Dimethylamine, N,N-Dimethylaniline , N,N-Dimethylformamide, Dimethyl phthalate, Dimethyl sulphate, 4,6-Dinitro-o-cresol , 2,4-Dinitrotoluene, Di-n-octyl phthalate, 1,4-Dioxane, Diphenylamine, Epichlorohydrin, 2-Ethoxyethanol, 2-Ethoxyethyl acetate, Ethyl acrylate, Ethylbenzene, Ethylene, Ethylene glycol, Ethylene oxide, Ethylene thiourea, Formaldehyde, Formic acid, HCFC-22, HCFC-122 (all isomers), HCFC-123 (all isomers), HCFC-124 (all isomers), HCFC-141b, HCFC-142b, Hexachlorocyclopentadiene, Hexachlorophene, n-Hexane, Hydroquinone, Isobutyraldehyde, Isophorone diisocyanate, Isopropyl alcohol, Maleic anhydride, 2-Mercaptobenzothiazole, Methanol, 2-Methoxyethanol, 2-(2-Methoxyethoxy)ethanol, 2-Methoxyethyl acetate, Methyl acrylate, Methyl tert-butyl ether, p,p′-Methylenebis(2-chloroaniline), 1,1-Methylenebis(4-isocyanatocyclohexane), Methylenebis(phenylisocyanate), p,p′-Methylenedianiline, Methyl ethyl ketone, Methyl iodide, Methyl isobutyl ketone, Methyl methacrylate, N-Methylolacrylamide, N-Methyl-2-pyrrolidone, Michler's ketone , Naphthalene, 2-Nitropropane, N-Nitrosodiphenylamine, Octylphenol and its ethoxylates, Peracetic acid , Phenol , p-Phenylenediamine , Phthalic anhydride, Polymeric diphenylmethane diisocyanate, Propionaldehyde, Propylene, Propylene oxide, Pyridine , Styrene, 1,1,1,2-Tetrachloroethane, 1,1,2,2-Tetrachloroethane, Tetrachloroethylene, Toluene, 1,2,4-Trichlorobenzene, 1,1,2-Trichloroethane, Trichloroethylene, Triethylamine, 1,2,4-Trimethylbenzene, 2,2,4-Trimethylhexamethylene diisocyanate, Vinyl acetate, Vinyl chloride, Xylene
Part 1: Group B Substances	Acrylonitrile, Bisphenol A, Chlorinated alkanes (medium-chain), Chlorinated alkanes (long-chain, Isoprene, Nonylphenol and its ethoxylates), Tetraethyl lead, Toluene-2,4-diisocyanate, Toluene-2,6-diisocyanate, Toluenediisocyanate (mixed isomers)
Part 5: VOCs with Additional Reporting Requirements[1]	Acetylene, Adipic acid, Benzene, 1,3-Butadiene, 2-Butoxyethanol, p-Dichlorobenzene, 1,2-Dichloroethane, Dimethylether, Ethanol, Ethyl acetate, Ethylene, Formaldehyde, Furfuryl alcohol, n-Hexane, Isopropyl alcohol, D-Limonene, Methanol, Methyl ethyl ketone, Methylcyclopentane, Methyl isobutyl ketone, Myrcene, beta-Phellandrene, alpha-Pinene, beta-Pinene, Propane, n-Propyl alcohol, Propylene, Styrene, Tetrahydrofuran, Toluene, 1,2,4-Trimethylbenzene, Vinyl acetate, Analytically unresolved hydrocarbons (C_{10} to C_{16+}), Heavy aromatic solvent naphtha, Hydrotreated heavy naphtha, Hydrotreated light distillate, Light aromatic solvent naphtha, Mineral spirits, Naphtha, Other glycol ethers and acetates, Propylene glycol methyl ether acetate, Solvent naphtha light aliphatic, Solvent naphtha medium aliphatic, Stoddard solvent, VM & P naphtha

Part 5: Isomer Groups	Butane, Butene, Butyl acetate, Cycloheptane, Cyclohexene, Cyclooctane, Decane, Ethyltoluene, Heptane, Hexane, Hexene, Nonane, Octane, Pentane, Pentene, Propyl acetate, Trimethylbenzene, Xylene

[1]Part 5 includes a set of CAS-specific chemical products (e.g., mineral spirits, Stoddard solvent, naphtha solvents) that include mixtures of VOCs and light IVOCs (i.e., C12-13), which while required, are not reported to the NPRI from oil sands facilities.

Table S4.[1] Formulae/compounds used in Fig. 1E.

VOC name (AWAS)	VOC Formula (AWAS)	Oxygenated VOC names (PTRMS+CIMS[2]; calibrated)	Oxygenated VOC formula example (PTRMS+CIMS; calibrated)
Ethene	C_2H_4	Formaldehyde	HCHO
Ethyne	C_2H_2	Methanol	CH_4O
Ethane	C_2H_6	Acetaldehyde	C_2H_4O
1-Propene	C_3H_6	Acrolein	C_3H_4O
Propane	C_3H_8	Acetone	C_3H_6O
Methane, chlorodifluoro-	$CHClF_2$	Methacrolein/MVK	C_4H_6O
Methane, dichlorodifluoro-	CCl_2F_2	Butanone	C_4H_8O
Methane, chloro-	CH_3Cl	Formic acid	CH_2O_2
Propane, 2-methyl-	C_4H_{10}	hydroxyacetonitrile	C_2H_3NO
Ethane, 1,2-dichloro-1,1,2,2-tetrafluoro-	$C_2H_4Cl_2$	Acetic acid	$C_2H_4O_2$
Ethene, chloro-	C_2H_3Cl	Nitroethanol	$C_2H_5NO_3$
1-Propene, 2-methyl- and 1-Butene	C_4H_8	Cyanoacetic acid	$C_3H_3NO_2$
1,3-Butadiene	C_4H_6	Acrylic acid	$C_3H_4O_2$
Butane	C_4H_{10}	Pyruvic acid	$C_3H_4O_3$
2-Butene, (2E)-	C_4H_8	Propanoic acid	$C_3H_6O_2$
Methane, bromo-	CH_3Br	Cyclopropane carboxylic acid	$C_4H_4O_2$
2-Butene, (2Z)-	C_4H_8	Methacrylic acid	$C_4H_6O_2$
Ethane, chloro-	C_2H_5Cl	3-oxobutanoic acid	$C_4H_6O_3$
1-Butene, 3-methyl-	C_5H_{10}	Butyric acid	$C_4H_8O_2$
Butane, 2-methyl-	C_5H_{12}	2-Hydroxybutyric acid	$C_4H_8O_3$
Methane, trichlorofluoro-	CCl_3F	2-Butenoic acid, 3-methyl-	$C_5H_8O_2$

1-Pentene	C_5H_{10}	Levulinic acid	$C_5H_8O_3$
1-Butene, 2-methyl-	C_5H_{10}	Valeric acid	$C_5H_{10}O_2$
Pentane	C_5H_{12}	3-Hydroxypentanoic acid	$C_5H_{10}O_3$
1,3-Butadiene, 2-methyl-	C_5H_8	cyclopentanoic acid	$C_6H_{10}O_2$
2-Pentene, (2E)-	C_5H_{10}	Hexanoic acid	$C_6H_{12}O_2$
Ethene, 1,1-dichloro-	$C_2H_2Cl_2$	Leucic acid	$C_6H_{12}O_3$
2-Pentene, (2Z)-	C_5H_{10}	1-Cyclohexenecarboxylic Acid	$C_7H_{10}O_2$
Methane, dichloro-	CH_2Cl_2	Heptenoic acid	$C_7H_{12}O_2$
2-Butene, 2-methyl-	C_5H_{10}	Heptanoic acid	$C_7H_{14}O_2$
Butane, 2,2-dimethyl-	C_6H_{14}	Isocyanic acid	HNCO
Ethane, 1,1-dichloro-	$C_2H_4Cl_2$		
Cyclopentane	C_5H_{10}		
Butane, 2,3-dimethyl-	C_6H_{14}		
Propane, 2-methoxy-2-methyl-	$C_5H_{12}O$		
Pentane, 2-methyl-	C_6H_{14}		
2-Pentene, 4-methyl-, (2E)-	C_6H_{12}		
Pentane, 3-methyl-	C_6H_{14}		
1-Hexene and 1-Pentene, 2-methyl-	C_6H_{12}		
Hexane	C_6H_{14}		
Methane, trichloro-	$CHCl_3$		
2-Hexene, (E)-	C_6H_{12}		
2-Pentene, 3-methyl-, (2E)-,	C_6H_{12}		
2-Hexene, (Z)	C_6H_{12}		
2-Pentene, 3-methyl-, (2Z)-	C_6H_{12}		
Ethane, 1,2-dichloro-	$C_2H_4Cl_2$		
Cyclopentane, methyl-	C_6H_{12}		

Pentane, 2,4-dimethyl-	C_7H_{16}
Ethane, 1,1,1-trichloro-	$C_2H_3Cl_3$
Benzene	C_6H_6
Methane, tetrachloro-	CCl_4
Cyclohexane	C_6H_{12}
Hexane, 2-methyl-	C_7H_{16}
Pentane, 2,3-dimethyl-	C_7H_{16}
Hexane, 3-methyl-	C_7H_{16}
Propane, 1,2-dichloro-	$C_3H_6Cl_2$
Ethene, trichloro-	C_2HCl_3
1-Heptene	C_7H_{14}
Pentane, 2,2,4-trimethyl-	C_8H_{18}
Heptane	C_7H_{16}
Cyclohexane, methyl-	C_7H_{14}
Hexane, 2,5-dimethyl-	C_8H_{18}
Hexane, 2,4-dimethyl-	C_8H_{18}
Ethane, 1,1,2-trichloro-	$C_2H_3Cl_3$
Pentane, 2,3,4-trimethyl-	C_8H_{18}
Benzene, methyl-	C_7H_8
Heptane, 2-methyl-	C_8H_{18}
Heptane, 4-methyl-	C_8H_{18}
Heptane, 3-methyl-	C_8H_{18}
Octane	C_8H_{18}
2-Octene, (2E)-	C_8H_{16}
Ethene, tetrachloro-	C_2Cl_4
Cyclohexane, 1,2-dimethyl-, (1R,2S)-rel-	C_8H_{16}
Benzene, chloro-	C_6H_5Cl

Benzene, ethyl-	C_8H_{10}
Benzene, 1,3(and 1,4)-dimethyl-	C_8H_{10}
Methane, tribromo-	$CHBr_3$
Benzene, ethenyl-	C_8H_{10}
Ethane, 1,1,2,2-tetrachloro-	$C_2H_2Cl_4$
Benzene, 1,2-dimethyl-	C_8H_{10}
Nonane	C_9H_{20}
Benzene, (1-methylethyl)-	C_9H_{12}
Bicyclo[3.1.1]hept-2-ene, 2,6,6-trimethyl-	$C_{10}H_{16}$
Benzene, propyl-	C_9H_{12}
Benzene, 1-ethyl-3-methyl-	C_9H_{12}
Bicyclo[2.2.1]heptane, 2,2-dimethyl-3-methylene-	$C_{10}H_{16}$
Benzene, 1-ethyl-4-methyl-	C_9H_{12}
Benzene, 1,3,5-trimethyl-	C_9H_{12}
Benzene, 1-ethyl-2-methyl-	C_9H_{12}
Bicyclo[3.1.1]heptane, 6,6-dimethyl-2-methylene-	$C_{10}H_{16}$
Benzene, 1,2,4-trimethyl-	C_9H_{12}
Benzene, (chloromethyl)-	C_7H_7Cl
Benzene, 1,3-dichloro-	$C_6H_4Cl_2$
Decane	$C_{10}H_{22}$
Benzene, 1,4-dichloro-	$C_6H_4Cl_2$
Benzene, 1,2,3-trimethyl-	C_9H_{12}
Benzene, 1-methyl-4-(1-methylethyl)-	$C_{10}H_{14}$
Benzene, 1,2-dichloro-	$C_6H_4Cl_2$
Cyclohexene, 1-methyl-4-(1-methylethenyl)-	$C_{10}H_{16}$

1H-Indene, 2,3-dihydro-	C_9H_9
Benzene, 1,3-diethyl-	$C_{10}H_{14}$
Benzene, 1,4-diethyl-	$C_{10}H_{14}$
Undecane[3]	$C_{11}H_{24}$
Benzene, 1,2,4-trichloro-	$C_6H_3Cl_3$
Naphthalene	$C_{10}H_8$
Dodecane[3]	$C_{12}H_{26}$
1,3-Butadiene, 1,1,2,3,4,4-hexachloro-	C_4Cl_6

[1]The fraction measured by PTR-MS+CIMS versus AWAS varies between samples. We have estimated this fraction for three major studied facilities: the PTR+CIMS measures 17-27% VOCs for Syncrude, 18-38% for Suncor, and 22-29% for CNRL. AWAS measured the remaining fraction of the VOCs.
[2]Additional oxidized species from PTR-MS and CIMS include $C_xH_yO_z$ and $C_xH_yN_zO_m$ (862 formulas).
[3]The linear alkanes n-undecane and n-dodecane are the only $C_{11\text{-}12}$ species included in the compound-specific measurements.

Table S5. Formulas corresponding to double bond equivalency (DBE) ratios.

DBE	Number of hydrogens based on C# (n)
0	2n+2
1	2n
2	2n-2
3	2n-4
4	2n-6
5	2n-8
6	2n-10
7	2n-12
8	2n-14
9	2n-16
10	2n-18
11	2n-20
12	2n-22
13	2n-24
14	2n-26
15	2n-28

Table S6. Average percent distribution (%) of mass concentrations across flight samples shown in Fig. 2B.

	Double bond equivalency															
C#	**0**	**1**	**2**	**3**	**4**	**5**	**6**	**7**	**8**	**9**	**10**	**11**	**12**	**13**	**14**	**15**
11	0.84	1.73	0.29	0.28	0.23	0.08	0.00	0.10	0.00	0.00	0.00	0.00	0.00	0.00	0.00	0.00
12	0.63	1.19	1.85	0.38	0.20	0.34	0.01	0.07	0.08	0.00	0.00	0.00	0.00	0.00	0.00	0.00
13	0.42	0.61	1.51	0.26	0.22	0.28	0.05	0.07	0.05	0.01	0.00	0.00	0.00	0.00	0.00	0.00
14	0.61	0.60	1.12	0.20	0.24	0.31	0.11	0.03	0.03	0.06	0.08	0.00	0.00	0.00	0.00	0.00
15	0.49	0.47	1.03	0.18	0.34	0.32	0.17	0.05	0.06	0.01	0.04	0.00	0.00	0.00	0.00	0.00
16	0.85	0.71	0.83	0.23	0.30	0.29	0.02	0.20	0.01	0.03	0.07	0.06	0.19	0.00	0.00	0.00
17	0.38	0.51	0.75	0.32	0.41	0.37	0.36	0.15	0.18	0.08	0.12	0.15	0.08	0.00	0.00	0.00
18	0.34	0.47	0.90	0.41	0.59	0.65	0.70	0.50	0.39	0.18	0.20	0.09	0.07	0.01	0.00	0.00
19	0.25	0.62	1.26	0.63	1.02	1.34	1.34	1.24	0.57	0.29	0.10	0.05	0.02	0.01	0.00	0.00
20	0.25	0.82	1.83	1.07	1.32	1.76	2.18	1.50	0.57	0.31	0.10	0.04	0.01	0.00	0.00	0.00
21	0.16	0.77	2.38	1.68	1.90	2.50	2.56	3.79	0.70	0.29	0.08	0.03	0.00	0.00	0.00	0.00
22	0.20	0.72	1.97	1.40	1.72	2.18	3.10	1.80	0.40	0.20	0.07	0.02	0.00	0.01	0.00	0.00
23	0.26	0.73	0.56	1.22	1.29	1.48	1.17	0.79	0.27	0.16	0.05	0.01	0.00	0.00	0.02	0.01
24	0.11	0.73	1.03	0.71	0.85	0.94	0.79	0.26	0.19	0.06	0.09	0.00	0.00	0.00	0.01	0.00
25	0.08	0.75	0.73	0.38	0.57	0.54	0.38	0.11	0.09	0.00	0.01	0.00	0.00	0.00	0.01	0.00

Table S7. I/SVOC emission factors from mature fine tailings samples used in Fig. 5A. Averages ± standard deviations are shown with ranges in parentheses with emissions measured in n-alkane equivalents. Measurements on the 11th day were taken before and after crust breaking, to simulate an industry practice to promote drying and also to examine the effect of changing surface conditions.

Sample	Emission factor ($mg\ min^{-1}\ kg^{-1}$)
Initial	3.73±0.55 (3.19-4.27)
4 hours	1.04±0.16 (0.91-1.16)
24 hours	0.77±0.12 (0.74-0.81)
4 days	10.5±0.40 (9.93-10.8)
11 days (pre-crust breaking)	7.89±0.24 (7.60-8.07)
11 days (post-crust breaking)	10.8±0.73 (10.1-11.5)
20 days	5.45±0.52 (4.94-5.95)
27 days	5.96±1.44 (4.26-7.77)
49 days	3.76±0.51 (3.07-4.23)
Irradiation before drying	1.94±1.07 (0.71-3.71)
Irradiation once dried	23.2±4.36 (15.1-28.2)

Table S8. Temperature dependence of I/SVOC emissions from dried tailings in Fig. 5B.
Averages ± standard deviations (in n-alkane equivalents) are shown with ranges in parentheses.

Temperature of sample (°C)	Emission factor (mg min^{-1} kg^{-1})
20	6.02±1.90 (4.15-8.61)
25	7.27±1.80 (5.16-9.56)
30	12.4±0.34 (12.2-12.9)
40	22.3±1.24 (21.0-23.9)
50	36.2±2.15 (33.3-38.5)

Table S9. Average percent distribution (Wt%) of mass concentrations across MFT off-gassing samples shown in Fig. 5D.

	Double bond equivalency															
C#	**0**	**1**	**2**	**3**	**4**	**5**	**6**	**7**	**8**	**9**	**10**	**11**	**12**	**13**	**14**	**15**
11	5.62	15.02	3.12	2.11	1.28	0.47	0.00	0.04	0.00	0.00	0.00	0.00	0.00	0.00	0.00	0.00
12	1.03	2.42	10.61	3.28	0.97	0.35	0.09	0.06	0.22	0.00	0.00	0.00	0.00	0.00	0.00	0.00
13	0.21	0.38	6.98	3.08	0.72	0.68	0.48	0.25	0.09	0.01	0.00	0.00	0.00	0.00	0.00	0.00
14	0.10	0.14	3.48	0.64	0.82	1.10	0.70	0.28	0.13	0.03	0.02	0.00	0.00	0.00	0.00	0.00
15	0.06	0.16	2.69	0.40	0.88	1.15	0.69	0.27	0.26	0.06	0.06	0.00	0.00	0.00	0.00	0.00
16	0.05	0.22	2.89	0.45	0.84	0.93	0.08	0.35	0.03	0.08	0.06	0.02	0.00	0.00	0.00	0.00
17	0.03	0.24	2.49	0.47	0.73	0.70	0.65	0.29	0.24	0.08	0.08	0.02	0.00	0.00	0.00	0.00
18	0.04	0.25	2.02	0.66	0.60	0.53	0.48	0.22	0.18	0.06	0.06	0.01	0.01	0.01	0.00	0.00
19	0.05	0.19	1.36	0.86	0.43	0.32	0.30	0.15	0.09	0.04	0.04	0.01	0.01	0.02	0.00	0.00
20	0.05	0.13	0.77	0.74	0.23	0.20	0.17	0.14	0.06	0.05	0.03	0.01	0.01	0.01	0.00	0.00
21	0.02	0.07	0.41	0.34	0.14	0.11	0.07	0.06	0.04	0.05	0.02	0.02	0.01	0.00	0.00	0.00
22	0.00	0.03	0.17	0.22	0.06	0.06	0.04	0.06	0.03	0.03	0.01	0.02	0.01	0.00	0.00	0.00
23	0.00	0.09	0.00	0.08	0.02	0.02	0.02	0.04	0.02	0.03	0.01	0.01	0.01	0.00	0.00	0.00
24	0.00	0.01	0.03	0.05	0.01	0.02	0.01	0.01	0.01	0.01	0.00	0.01	0.00	0.00	0.00	0.00
25	0.00	0.03	0.01	0.00	0.00	0.00	0.01	0.00	0.00	0.00	0.00	0.00	0.00	0.00	0.00	0.00

Table S10. Average percent distribution (Wt%) of mass concentrations across MFT off-gassing samples shown in Fig. S14.

	Double bond equivalency															
C#	**0**	**1**	**2**	**3**	**4**	**5**	**6**	**7**	**8**	**9**	**10**	**11**	**12**	**13**	**14**	**15**
11	5.52	16.89	2.72	4.31	1.30	0.58	0.00	0.02	0.00	0.00	0.00	0.00	0.00	0.00	0.00	0.00
12	1.17	2.59	11.48	7.88	0.93	0.40	0.06	0.03	0.07	0.00	0.00	0.00	0.00	0.00	0.00	0.00
13	0.36	0.40	8.38	5.75	0.72	0.72	0.27	0.09	0.03	0.00	0.00	0.00	0.00	0.00	0.00	0.00
14	0.15	0.15	3.94	1.27	0.80	1.00	0.39	0.07	0.03	0.01	0.01	0.00	0.00	0.00	0.00	0.00
15	0.09	0.18	2.61	0.76	0.76	0.85	0.42	0.07	0.06	0.01	0.01	0.00	0.00	0.00	0.00	0.00
16	0.07	0.18	2.29	0.83	0.61	0.50	0.04	0.08	0.01	0.01	0.01	0.00	0.00	0.00	0.00	0.00
17	0.05	0.19	1.52	0.73	0.37	0.27	0.22	0.06	0.03	0.01	0.01	0.00	0.00	0.00	0.00	0.00
18	0.08	0.13	0.83	0.87	0.21	0.15	0.12	0.04	0.02	0.01	0.01	0.00	0.00	0.00	0.00	0.00
19	0.07	0.06	0.41	0.90	0.12	0.07	0.04	0.02	0.01	0.01	0.01	0.00	0.00	0.00	0.00	0.00
20	0.08	0.03	0.18	0.47	0.05	0.04	0.02	0.03	0.01	0.01	0.00	0.01	0.00	0.00	0.00	0.00
21	0.00	0.00	0.07	0.21	0.02	0.02	0.00	0.00	0.01	0.01	0.00	0.00	0.00	0.00	0.00	0.00
22	0.00	0.00	0.01	0.03	0.00	0.01	0.00	0.01	0.00	0.00	0.00	0.00	0.00	0.00	0.00	0.00
23	0.00	0.00	0.00	0.00	0.00	0.00	0.00	0.00	0.00	0.00	0.00	0.00	0.00	0.00	0.00	0.00
24	0.00	0.00	0.00	0.00	0.00	0.00	0.00	0.00	0.00	0.00	0.00	0.00	0.00	0.00	0.00	0.00
25	0.00	0.00	0.00	0.00	0.00	0.00	0.00	0.00	0.00	0.00	0.00	0.00	0.00	0.00	0.00	0.00

References and Notes

1. Y. Zhao, C. J. Hennigan, A. A. May, D. S. Tkacik, J. A. de Gouw, J. B. Gilman, W. C. Kuster, A. Borbon, A. L. Robinson, Intermediate-volatility organic compounds: A large source of secondary organic aerosol. *Environ. Sci. Technol.* **48**, 13743–13750 (2014).

2. E. N. Kelly, J. W. Short, D. W. Schindler, P. V. Hodson, M. Ma, A. K. Kwan, B. L. Fortin, Oil sands development contributes polycyclic aromatic compounds to the Athabasca River and its tributaries. *Proc. Natl. Acad. Sci. U.S.A.* **106**, 22346–22351 (2009).

3. I. J. Simpson, N. J. Blake, B. Barletta, G. S. Diskin, H. E. Fuelberg, K. Gorham, L. G. Huey, S. Meinardi, F. S. Rowland, S. A. Vay, A. J. Weinheimer, M. Yang, D. R. Blake, Characterization of trace gases measured over alberta oil sands mining operations: 76 speciated C_2-C_{10} volatile organic compounds (VOCs), CO_2, CH_4, CO, NO, NO_2, NOy, O_3 and SO_2. *Atmos. Chem. Phys.* **10**, 11931–11954 (2010).

4. J. L. Jimenez, M. R. Canagaratna, N. M. Donahue, A. S. H. Prevot, Q. Zhang, J. H. Kroll, P. F. DeCarlo, J. D. Allan, H. Coe, N. L. Ng, A. C. Aiken, K. S. Docherty, I. M. Ulbrich, A. P. Grieshop, A. L. Robinson, J. Duplissy, J. D. Smith, K. R. Wilson, V. A. Lanz, C. Hueglin, Y. L. Sun, J. Tian, A. Laaksonen, T. Raatikainen, J. Rautiainen, P. Vaattovaara, M. Ehn, M. Kulmala, J. M. Tomlinson, D. R. Collins, M. J. Cubison, E. J. Dunlea, J. A. Huffman, T. B. Onasch, M. R. Alfarra, P. I. Williams, K. Bower, Y. Kondo, J. Schneider, F. Drewnick, S. Borrmann, S. Weimer, K. Demerjian, D. Salcedo, L. Cottrell, R. Griffin, A. Takami, T. Miyoshi, S. Hatakeyama, A. Shimono, J. Y. Sun, Y. M. Zhang, K. Dzepina, J. R. Kimmel, D. Sueper, J. T. Jayne, S. C. Herndon, A. M. Trimborn, L. R. Williams, E. C. Wood, A. M. Middlebrook, C. E. Kolb, U. Baltensperger, D. R. Worsnop, Evolution of organic aerosols in the atmosphere. *Science* **326**, 1525–1529 (2009).

5. S. Feng, D. Gao, F. Liao, F. Zhou, X. Wang, The health effects of ambient PM2.5 and potential mechanisms. *Ecotoxicol. Environ. Saf.* **128**, 67–74 (2016).

6. S. Fuzzi *et al*., Particulate matter, air quality and climate: Lessons learned and future needs. *Atmos. Chem. Phys.* **15**, 8217–8299 (2015).

7. D. R. Gentner, G. Isaacman, D. R. Worton, A. W. H. Chan, T. R. Dallmann, L. Davis, S. Liu, D. A. Day, L. M. Russell, K. R. Wilson, R. Weber, A. Guha, R. A. Harley, A. H. Goldstein, Elucidating secondary organic aerosol from diesel and gasoline vehicles through detailed characterization of organic carbon emissions. *Proc. Natl. Acad. Sci. U.S.A.* **109**, 18318–18323 (2012).

8. Q. Lu, Y. Zhao, A. L. Robinson, Comprehensive organic emission profiles for gasoline, diesel, and gas-turbine engines including intermediate and semi-volatile organic compound emissions. *Atmos. Chem. Phys.* **18**, 17637–17654 (2018).

9. G. Pétron, A. Karion, C. Sweeney, B. R. Miller, S. A. Montzka, G. J. Frost, M. Trainer, P. Tans, A. Andrews, J. Kofler, D. Helmig, D. Guenther, E. Dlugokencky, P. Lang, T. Newberger, S. Wolter, B. Hall, P. Novelli, A. Brewer, S. Conley, M. Hardesty, R. Banta, A. White, D. Noone, D. Wolfe, R. Schnell, A new look at methane and nonmethane hydrocarbon emissions from oil and natural gas operations in the Colorado Denver-Julesburg Basin. *J. Geophys. Res. Atmos.* **119**, 6836–6852 (2014).

10. J. Liggio, S.-M. Li, K. Hayden, Y. M. Taha, C. Stroud, A. Darlington, B. D. Drollette, M. Gordon, P. Lee, P. Liu, A. Leithead, S. G. Moussa, D. Wang, J. O'Brien, R. L. Mittermeier, J. R. Brook, G. Lu, R. M. Staebler, Y. Han, T. W. Tokarek, H. D. Osthoff, P. A. Makar, J. Zhang, D. L. Plata, D. R. Gentner, Oil sands operations as a large source of secondary organic aerosols. *Nature* **534**, 91–94 (2016).

11. L. Rosa, K. F. Davis, M. C. Rulli, P. D'Odorico, Environmental consequences of oil production from oil sands. *Earths Futur.* **5**, 158–170 (2017).

12. Government of Alberta, "Environmental management of Alberta's oil sands" (2009); https://open.alberta.ca/publications/9780778576778

13. Alberta Energy Regulator, "Crude Bitumen - In Situ Production" (2023); https://www.aer.ca/providing-information/data-and-reports/statistical-reports/st98/crude-bitumen/production/in-situ.

14. Alberta Energy Regulator, "ST3: Alberta Energy Resource Industries Monthly Statistics" (2017); https://www.aer.ca/providing-information/data-and-reports/statistical-reports/st3.

15. S. M. Li, A. Leithead, S. G. Moussa, J. Liggio, M. D. Moran, D. Wang, K. Hayden, A. Darlington, M. Gordon, R. Staebler, P. A. Makar, C. A. Stroud, R. McLaren, P. S. K. Liu, J. O'Brien, R. L. Mittermeier, J. Zhang, G. Marson, S. G. Cober, M. Wolde, J. J. B. Wentzell, Differences between measured and reported volatile organic compound emissions from oil sands facilities in Alberta, Canada. *Proc. Natl. Acad. Sci. U.S.A.* **114**, E3756–E3765 (2017).

16. J. Liggio, S. G. Moussa, J. Wentzell, A. Darlington, P. Liu, A. Leithead, K. Hayden, J. O'Brien, R. L. Mittermeier, R. Staebler, M. Wolde, S.-M. Li, Understanding the primary emissions and secondary formation of gaseous organic acids in the oil sands region of Alberta, Canada. *Atmos. Chem. Phys.* **17**, 8411–8427 (2017).

17. J. R. Brook, S. G. Cober, M. Freemark, T. Harner, S. M. Li, J. Liggio, P. Makar, B. Pauli, Advances in science and applications of air pollution monitoring: A case study on oil sands monitoring targeting ecosystem protection. *J. Air Waste Manag. Assoc.* **69**, 661–709 (2019).

18. K. L. Hayden, S.-M. Li, J. Liggio, M. J. Wheeler, J. J. B. Wentzell, A. Leithead, P. Brickell, R. L. Mittermeier, Z. Oldham, C. M. Mihele, R. M. Staebler, S. G. Moussa, A. Darlington, M. Wolde, D. Thompson, J. Chen, D. Griffin, E. Eckert, J. C. Ditto, M. He, D. R. Gentner, Reconciling the total carbon budget for boreal forest wildfire emissions using airborne observations. *Atmos. Chem. Phys.* **22**, 12493–12523 (2022).

19. M. Gordon, S.-M. Li, R. Staebler, A. Darlington, K. Hayden, J. O'Brien, M. Wolde, Determining air pollutant emission rates based on mass balance using airborne measurement data over the Alberta oil sands operations. *Atmos. Meas. Tech.* **8**, 3745–3765 (2015).

20. J. Liggio, S.-M. Li, R. M. Staebler, K. Hayden, A. Darlington, R. L. Mittermeier, J. O'Brien, R. McLaren, M. Wolde, D. Worthy, F. Vogel, Measured Canadian oil sands CO_2 emissions are higher than estimates made using internationally recommended methods. *Nat. Commun.* **10**, 1863 (2019).

21. B. M. Erland, C. Adams, A. Darlington, M. L. Smith, A. K. Thorpe, G. R. Wentworth, S. Conley, J. Liggio, S.-M. Li, C. E. Miller, J. A. Gamon, Comparing airborne algorithms for greenhouse gas flux measurements over the Alberta oil sands. *Atmos. Meas. Tech.* **15**, 5841–5859 (2022).

22. A. D. Charpentier, J. A. Bergerson, H. L. MacLean, Understanding the Canadian oil sands industry's greenhouse gas emissions. *Environ. Res. Lett.* **4**, 014005 (2009).

23. Alberta Energy Regulator, "Statistical Series 39 Alberta Mineable Oil Sands Plant Statistics Monthly Supplement" (2018); https://static.aer.ca/prd/documents/sts/ST39-2018.pdf.

24. J. Peischl, S. J. Eilerman, J. A. Neuman, K. C. Aikin, J. de Gouw, J. B. Gilman, S. C. Herndon, R. Nadkarni, M. Trainer, C. Warneke, T. B. Ryerson, Quantifying Methane and Ethane Emissions to the Atmosphere From Central and Western U.S. Oil and Natural Gas Production Regions. *J. Geophys. Res. Atmos.* **123**, 7725–7740 (2018).

25. Environment and Climate Change Canada, "National Pollutant Release Inventory" (2019); https://pollution-waste.canada.ca/national-release-inventory/archives/index.cfm?lang=en.

26. Government of Alberta, "Alberta Emissions Inventory Report (AEIR) Air Emission Rates" (2020); https://open.alberta.ca/opendata/aeirairemissionrates#summary.

27. I. B. Konovalov, E. V. Berezin, P. Ciais, G. Broquet, R. V. Zhuravlev, G. Janssens-Maenhout, Estimation of fossil-fuel CO_2 emissions using satellite measurements of "proxy" species. *Atmos. Chem. Phys.* **16**, 13509–13540 (2016).

28. F. Liu, B. N. Duncan, N. A. Krotkov, L. N. Lamsal, S. Beirle, D. Griffin, C. A. McLinden, D. L. Goldberg, Z. Lu, A methodology to constrain carbon dioxide emissions from coal-fired power plants using satellite observations of co-emitted nitrogen dioxide. *Atmos. Chem. Phys.* **20**, 99–116 (2020).

29. S. N. Wren, C. A. McLinden, D. Griffin, S.-M. Li, S. G. Cober, A. Darlington, K. Hayden, C. Mihele, R. L. Mittermeier, M. J. Wheeler, M. Wolde, J. Liggio, Aircraft and satellite observations reveal historical gap between top-down and bottom-up CO_2 emissions from Canadian oil sands. *PNAS Nexus* **2**, pgad140 (2023).

30. Environment and Climate Change Canada, "Canada's Air Pollutant Emissions Inventory" (2018); https://data-donnees.ec.gc.ca/data/substances/monitor/canada-s-air-pollutant-emissions-inventory.

31. Alberta Energy Regulator, "ST53: Alberta In Situ Oil Sands Production Summary" (2018); https://www.aer.ca/providing-information/data-and-reports/statistical-reports/st53.

32. O. P. Strausz, A. Morales-Izquierdo, N. Kazmi, D. S. Montgomery, J. D. Payzant, I. Safarik, J. Murgich, Chemical composition of Athabasca bitumen: The saturate fraction. *Energy Fuels* **24**, 5053–5072 (2010).

33. L. He, X. Li, G. Wu, F. Lin, H. Sui, Distribution of Saturates, Aromatics, resins, and asphaltenes fractions in the bituminous layer of athabasca oil sands. *Energy Fuels* **27**, 4677–4683 (2013).

34. M. H. Erickson, M. Gueneron, B. T. Jobson, Measuring long chain alkanes in diesel engine exhaust by thermal desorption PTR-MS. *Atmos. Meas. Tech.* **7**, 225–239 (2014).

35. J. C. Ditto, M. He, T. N. Hass-Mitchell, S. G. Moussa, K. Hayden, S.-M. Li, J. Liggio, A. Leithead, P. Lee, M. J. Wheeler, J. J. B. Wentzell, D. R. Gentner, Atmospheric evolution of emissions from a boreal forest fire: The formation of highly functionalized oxygen-, nitrogen-, and sulfur-containing organic compounds. *Atmos. Chem. Phys.* **21**, 255–267 (2021).

36. California Air Resources Board, "2015 Estimated Annual Average Emissions Statewide" (2016); https://www.arb.ca.gov/app/emsinv/2017/emseic1p_query.php.

37. B. D. Drollette, D. R. Gentner, D. L. Plata, Waste Containment Ponds Are a Major Source of Secondary Organic Aerosol Precursors from Oil Sands Operations. *Environ. Sci. Technol.* **54**, 9872–9881 (2020).

38. Alberta Energy Regulator, "State of Fluid Tailings Management for Mineable Oil Sands, 2020" (2021); https://static.aer.ca/prd/documents/reports/2020-State-Fluid-Tailings-Management-Mineable-OilSands.pdf.

39. Canadian Natural Upgrading, "Canadian Natural Muskeg River Mine Fluid Tailings Management Report" (Canadian Natural Upgrading, 2020); https://www.aer.ca/providing-information/by-topic/tailings.

40. Alberta Energy Regulator, "State of Fluid Tailings Management for Mineable Oil Sands, 2018" (2019); https://static.aer.ca/prd/documents/oilsands/2018-State-Fluid-Tailings-Management-Mineable-OilSands.pdf.

41. California Air Resources Board, "CEPAM2019v1.03 Emission Projection Data 2017: Estimated Annual Average Emissions Los Angeles County" (2017); https://ww2.arb.ca.gov/applications/emissions-county.

42. Environment and Climate Change Canada, "2018 National Pollutant Release Inventory (NPRI) Facility-Reported Data" (2018); https://www.canada.ca/en/services/environment/pollution-waste-management/national-pollutant-release-inventory.html.

43. G. Chow-Fraser, A. Rougeot, *50 Years of Sprawling Tailings: Mapping Decades of Destruction by Oil Sands Tailings* (CPAWS Northern Alberta, Environmental Defence Canada, 2022).

44. B. A. Nault, D. S. Jo, B. C. McDonald, P. Campuzano-Jost, D. A. Day, W. Hu, J. C. Schroder, J. Allan, D. R. Blake, M. R. Canagaratna, H. Coe, M. M. Coggon, P. F. DeCarlo, G. S. Diskin, R. Dunmore, F. Flocke, A. Fried, J. B. Gilman, G. Gkatzelis, J. F. Hamilton, T. F. Hanisco, P. L. Hayes, D. K. Henze, A. Hodzic, J. Hopkins, M. Hu, L. G. Huey, B. T. Jobson, W. C. Kuster, A. Lewis, M. Li, J. Liao, M. O. Nawaz, I. B. Pollack, J. Peischl, B. Rappenglück, C. E. Reeves, D. Richter, J. M. Roberts, T. B. Ryerson, M. Shao, J. M. Sommers, J. Walega, C. Warneke, P. Weibring, G. M. Wolfe, D. E. Young, B. Yuan, Q. Zhang, J. A. de Gouw, J. L. Jimenez, Secondary organic aerosols from anthropogenic volatile organic compounds contribute substantially to air pollution mortality. *Atmos. Chem. Phys.* **21**, 11201–11224 (2021).

45. A. Hodzic, J. L. Jimenez, S. Madronich, M. R. Canagaratna, P. F. DeCarlo, L. Kleinman, J. Fast, Modeling organic aerosols in a megacity: Potential contribution of semi-volatile and

intermediate volatility primary organic compounds to secondary organic aerosol formation. *Atmos. Chem. Phys.* **10**, 5491–5514 (2010).

46. C. E. Stockwell, A. Kupc, B. Witkowski, R. K. Talukdar, Y. Liu, V. Selimovic, K. J. Zarzana, K. Sekimoto, C. Warneke, R. A. Washenfelder, R. J. Yokelson, A. M. Middlebrook, J. M. Roberts, Characterization of a catalyst-based conversion technique to measure total particulate nitrogen and organic carbon and comparison to a particle mass measurement instrument. *Atmos. Meas. Tech.* **11**, 2749–2764 (2018).

47. P. Veres, J. M. Roberts, I. R. Burling, C. Warneke, J. de Gouw, R. J. Yokelson, Measurements of gas-phase inorganic and organic acids from biomass fires by negative-ion proton-transfer chemical-ionization mass spectrometry. *J. Geophys. Res.* **115**, 2010JD014033 (2010).

48. K. Li, J. J. B. Wentzell, Q. Liu, A. Leithead, S. G. Moussa, M. J. Wheeler, C. Han, P. Lee, S.-M. Li, J. Liggio, Evolution of atmospheric total organic carbon from petrochemical mixtures. *Environ. Sci. Technol.* **55**, 12841–12851 (2021).

49. A. R. Koss, K. Sekimoto, J. B. Gilman, V. Selimovic, M. M. Coggon, K. J. Zarzana, B. Yuan, B. M. Lerner, S. S. Brown, J. L. Jimenez, J. Krechmer, J. M. Roberts, C. Warneke, R. J. Yokelson, J. de Gouw, Non-methane organic gas emissions from biomass burning: Identification, quantification, and emission factors from PTR-ToF during the FIREX 2016 laboratory experiment. *Atmos. Chem. Phys.* **18**, 3299–3319 (2018).

50. W. Permar, Q. Wang, V. Selimovic, C. Wielgasz, R. J. Yokelson, R. S. Hornbrook, A. J. Hills, E. C. Apel, I.-T. Ku, Y. Zhou, B. C. Sive, A. P. Sullivan, J. L. Collett Jr., T. L. Campos, B. B. Palm, Q. Peng, J. A. Thornton, L. A. Garofalo, D. K. Farmer, S. M. Kreidenweis, E. J. T. Levin, P. J. DeMott, F. Flocke, E. V. Fischer, L. Hu, Emissions of trace organic gases from western U.S. wildfires based on WE-CAN aircraft measurements. *J. Geophys. Res. Atmos.* **126**, e2020JD033838 (2021).

51. R. Sheu, A. Marcotte, P. Khare, S. Charan, J. C. Ditto, D. R. Gentner, Advances in offline approaches for chemically speciated measurements of trace gas-phase organic compounds via adsorbent tubes in an integrated sampling-to-analysis system. *J. Chromatogr. A* **1575**, 80–90 (2018).

52. P. Khare, A. Marcotte, R. Sheu, A. N. Walsh, J. C. Ditto, D. R. Gentner, Advances in offline approaches for trace measurements of complex organic compound mixtures via soft ionization and high-resolution tandem mass spectrometry. *J. Chromatogr. A* **1598**, 163–174 (2019).

53. D. R. Worton, H. Zhang, G. Isaacman-VanWertz, A. W. H. Chan, K. R. Wilson, A. H. Goldstein, Comprehensive chemical characterization of hydrocarbons in NIST Standard Reference Material 2779 Gulf of Mexico crude oil. *Environ. Sci. Technol.* **49**, 13130–13138 (2015).

54. S. Fathi, M. Gordon, P. A. Makar, A. Akingunola, A. Darlington, J. Liggio, K. Hayden, S.-M. Li, Evaluating the impact of storage-and-release on aircraft-based mass-balance methodology using a regional air-quality model. *Atmos. Chem. Phys.* **21**, 15461–15491 (2021).

55. K. L. Hayden, S.-M. Li, P. Makar, J. Liggio, S. G. Moussa, A. Akingunola, R. McLaren, R. M. Staebler, A. Darlington, J. O'Brien, J. Zhang, M. Wolde, L. Zhang, New methodology shows short atmospheric lifetimes of oxidized sulfur and nitrogen due to dry deposition. *Atmos. Chem. Phys.* **21**, 8377–8392 (2021).

56. S. Baray, A. Darlington, M. Gordon, K. L. Hayden, A. Leithead, S.-M. Li, P. S. K. Liu, R. L. Mittermeier, S. G. Moussa, J. O'Brien, R. Staebler, M. Wolde, D. Worthy, R. McLaren, Quantification of methane sources in the Athabasca Oil Sands Region of Alberta by aircraft mass balance. *Atmos. Chem. Phys.* **18**, 7361–7378 (2018).

57. J. A. de Gouw, J. B. Gilman, S.-W. Kim, S. L. Alvarez, S. Dusanter, M. Graus, S. M. Griffith, G. Isaacman-VanWertz, W. C. Kuster, B. L. Lefer, B. M. Lerner, B. C. McDonald, B. Rappenglück, J. M. Roberts, P. S. Stevens, J. Stutz, R. Thalman, P. R. Veres, R. Volkamer, C. Warneke, R. A. Washenfelder, C. J. Young, Chemistry of volatile organic compounds in the Los Angeles basin: Formation of oxygenated compounds and determination of emission ratios. *J. Geophys. Res. Atmos.* **123**, 2298–2319 (2018).

58. Government of Alberta, "Lower Athabasca Region Tailings Management Framework for Mineable Athabasca Oil Sands (TMF)" (2015); https://open.alberta.ca/dataset/962bc8f4-3924-46ce-baf8-d6b7a26467ae/resource/7c49eb63-751b-49fd-b746-87d5edee3131/download/2015-larp-tailingsmgtathabascaoilsands.pdf.

59. Fine Fluid Tailings Explained, *Oil Sands Magazine* 11 May 2023; https://www.oilsandsmagazine.com/news/2023/5/11/fine-fluid-tailings-explained-problems-solutions.

60. Syncrude, "2020 Sustainability Fact Sheet: Tailings" (2021); https://syncrude.ca/wp-content/uploads/2021/09/Fact-Sheet-_Tailings-2020.pdf.

61. Canada's Oil & Natural Gas Producers (CAPP), "Oil Sands Tailings" (2023); https://www.capp.ca/explore/tailings-ponds.

62. Alberta Energy Regulator, *Decision 20171025A: Suncor Energy Inc* (Applications for Millennium Operational Amendment and Base Plant Tailings Management Plan, 2017).

63. J.G. Matthews, W.H. Shaw, M. D. MacKinnon, R.G. Cuddy, Development of composite tailings technology at Syncrude. *Int. J. Surf. Mining. Reclam. Environ.* **16**, 24–39 (2002).

64. Oil Sands Tailings Consortium (OSTC), "Technical Guide for Fluid Fine Tailings Management" (OSTC, 2012).

65. P. Khare, J. Machesky, R. Soto, M. He, A. A. Presto, D. R. Gentner, Asphalt-related emissions are a major missing nontraditional source of secondary organic aerosol precursors. *Sci. Adv.* **6**, eabb9785 (2020).

66. M. L. Chacón-Patiño, S. F. Niles, A. G. Marshall, C. L. Hendrickson, R. P. Rodgers, Role of molecular structure in the production of water-soluble species by photo-oxidation of petroleum. *Environ. Sci. Technol.* **54**, 9968–9979 (2020).

67. S. F. Niles, M. L. Chacón-Patiño, S. P. Putnam, R. P. Rodgers, A. G. Marshall, Characterization of an asphalt binder and photoproducts by Fourier transform ion cyclotron resonance mass spectrometry reveals abundant water-soluble hydrocarbons. *Environ. Sci. Technol.* **54**, 8830–8836 (2020).

68. Alberta Energy Regulator, “State of Fluid Tailings Management for Mineable Oil Sands, 2022” (Alberta Energy Regulator, 2023).

69. R. G. Pillai, N. Yang, S. Thi, J. Fatema, M. Sadrzadeh, D. Pernitsky, Characterization and comparison of dissolved organic matter signatures in steam-assisted gravity drainage process water samples from Athabasca oil sands. *Energy Fuels* **31**, 8363–8373 (2017).

70. Government of Canada, *Canada Gazette* **156** (suppl.), 7 (2022); https://www.gazette.gc.ca/rp-pr/p1/2022/2022-02-12/html/sup1-eng.html.